

Quasiparticle states of hexagonal BN: A van der Waals density functional study

Raul Quintero-Monsebaiz* and Per Hyldgaard†

Microtechnology and Nanoscience, MC2, Chalmers University of Technology, SE-412 96 Göteborg, Sweden

(Dated: November 21, 2025)

We compute and track the impact of truly nonlocal-correlation effects on the quasi-particle (QP) band-structure of hexagonal boron-nitride (h-BN) systems. To that end, we start with the consistent-exchange vdW-DF-cx version [PRB **89**, 035412 (2014)] of the van der Waals density functional (vdW-DF) method [JPCM **39**, 390001 (2020)] for exchange-correlation (XC) functional design and enforce piece-wise linearity in the energy changes with partial charging, using the Koopmans-integer (KI) DFT framework [JCTC **19**, 7079 (2023)]. Our approach and results (denoted KI-CX) extends present-standard use of KI DFT (denoted KI-PBE as it is based on the semilocal PBE [PRL **77**, 3865 (1996)] XC functional) to capture, for example, the impact of the interlayer coupling on the QPs. We contrast KI-CX and KI-PBE results for the QP band-structure and compare with both *GW* calculations and experimental observations of the (direct and indirect) QP gaps. We find that KI-CX brings improvements in the h-BN QP energy description and generally agrees with *GW* studies.

I. INTRODUCTION

The goal of improving materials predictions by parameter-free theory prompts us to seek deeper understanding of sudden charged excitations in light-matter interactions and of ground state (GS) properties in concert. For the former, we can summarize the nature of such excitations as quasi-particle (QP) states, whose energies and spatial variation reflect the characteristics of the electronic-structure changes [1–3] upon photon absorption or emission. Formally exact many body perturbation theory (MBPT), for example, in the GWT [4, 5] or equation-of-motion coupled-cluster [6–9] (EOMCC) approaches, permit us to predict the QPs as solutions to effective dynamics problems. Meanwhile, for GS properties, formally exact density functional theory [10] (DFT), using either the traditional and popular Kohn-Sham (KS) [11–14], the generalized-KS [15–23], or the various Koopmans [24–30] DFT frameworks, can predict the atomic structure and the electron-density variations. DFT also relies on an equation-of-motion framework but for fictitious independent particles in an effective local potential that reflects enough of the QP dynamics that we can compute the GS electron behavior [31–35].

In practice, we need MBPT input to define robust so-called exchange-correlation (XC) functional approximations [34–46]. Approximations also enter MBPT-based QP studies (e.g., in *GW* [5]) and we seek consistency in XC design work [23, 25, 32–35, 41, 47]. Progress in such a concerted approach should and can be tested on both GS and QP properties [21, 23, 48, 49].

With an accurate XC functional approximation, KS-DFT lets us predict the atomic configurations [14] and materials vibrations, e.g., Refs. [50, 51]. Such computational characterizations permit theory validation both directly (on thermophysical properties and phases, e.g.,

Ref. [52]) and indirectly on the QPs, as revealed in electrical transport measurements [53], scanning tunneling microscopy (STM) [54], angle-resolved photoemission (ARPES) [55, 56], or inverse photoemission [57]. These properties generally reflect the QP band structure (energy variation with momentum in an extended system). In terms of MBPT and XC quality testing, one key observation is that (sub-)picometer accuracy at atomic structure characterization is typically required to, in turn, accurately predict the light-matter interactions in the more costly MBPT methods [3].

Notably, direct theory-experiment testing on QPs has a higher value still for materials-theory development. We observe that Koopmans-integer (KI) DFT [26–29, 49], using a linear-response description based on a given input XC functional, stands out by providing fast QP predictions without changing neither total energies nor the forces that set structure when that XC input is used in KS-DFT [29]. Accurate tools, linking the structure and QP aspects of materials modeling, are valuable for characterizations in their own rights but KI-DFT offers a potential for synergy in continued method developments. The structure of the Hedin QP-equation-of-motion framework is equivalent to the formal adiabatic-connection formula (ACF) specification of the XC functional designs [32, 35, 45]. For a versatile XC functional, and certainly when used for layered materials, we expect to find fingerprints of, for example, van der Waals (vdW) interactions on the QPs band structure, that is, in the energy variation with the QP momentum. We can test, for example, the accuracy of an XC choice on descriptions of the interlayer vdW attractions by comparing the corresponding QP predictions by KI-DFT to either measurements or direct MBPT characterizations.

Present-standard KI-DFT studies [26–29, 49, 58–65], rely on either the local-density approximation (LDA) [32, 66] or the the semilocal Perdew-Burke-Ernzerhof (PBE) [45] XC functional. The latter of these functionals is developed for KS-DFT and gives what we here label as PBE results. Via an extension to density functional

* raulq@chalmers.se

† hyldgaar@chalmers.se

perturbation theory (DFPT), PBE also permits efficient QP characterizations in what we call KI-PBE, when a piecewise-linearity (PWL) constraint [24, 29, 49, 67, 68] is imposed on the energy variation with partial charging. However, KI-DFT still reflects the nature of the XC functional that is chosen for KI-DFT [29] and KI-PBE is not set up to track vdW interactions [35]. This holds also for KI-PBE predictions of the QP band structure characterization, that is, in the QP energy variation with momentum.

It is motivated to move KI-DFT usage to instead start from a truly nonlocal-correlation functional form, available within the vdW density functional (vdW-DF) method [23, 35, 46, 69–74]. Stacking multiple layers of a two-dimensional material to form a bulk system is known to alter its band structure [75]. An expansion that reflects an incorrect structure prediction of the interlayer spacing, will induce further changes [76]. Beyond those observations is again the fact that QPs are the most direct way that we can test the quality of the QP and MBPT logic behind many of our XC functionals designs [32–35, 45, 70, 71, 77, 78].

Here we therefore present a study tracking vdW signatures on QPs in hexagonal boron-nitride systems (h-BN) while introducing the use of KI-CX, that is, KI-DFT with a start in the consistent-exchange vdW-DF-cx version (here abbreviated CX) [35, 78, 79]. We note that the QUANTUMESPRESSO (QE) suite of DFT codes [80, 81], with the module for KOOPMANS-DFT extension [29, 30], is already set up for KI-CX studies. The h-BN systems are insulating and have been thoroughly studied both theoretically and experimentally. h-BN has emerged as one of the most prominent two-dimensional materials, owing in part to a graphene-like honeycomb structure in its layers and to its wide band gap [82, 83]. Additionally, h-BN exhibits a suite of advantageous properties, such as excellent thermal conductivity [84], unique thickness-dependent behavior [85], chemical stability [86], optical functionality [87], and polymer compatibility [88]. These attributes enable applications in aerospace [86, 89], environmental science, and energy technologies—spanning adsorption, photo-catalysis, membrane separation, disinfection, environmental sensing, as well as energy conversion and storage [90].

The QPs correspond to sudden events that may be either adding or removing an electron [1]. We focus on QPs in three systems that are experimentally available, and we first set the atomic structure by observations. This means that KI-CX versus KI-PBE differences reflect the direct impacts of truly nonlocal-correlation effects (interlayer coupling) on the QPs. We next track the full impact of including nonlocal-correlations (via KI-CX) on the QP description. This is done by also contrasting KI-CX and KI-PBE QP descriptions at the structure predictions provided by these XC functional choices (namely, using CX and PBE in KS-DFT, respectively). There are local and global valence-band (conduction-band) extrema, together forming a number of (indirect) QP gaps

in h-BN systems. We assess KI-PBE and KI-CX quality on accuracy for those gaps, comparing with experimental observations and GW studies.

The manuscript is structured as follows. The following two sections summarizes the CX functional and use of KI-DFT, including computational parameters, input configurations, and work flows. Our results and discussion section presents and interprets KI-CX versus KI-PBE performance differences. Section V contains our summary and outlook. The paper contains two appendices.

II. THEORY

In this section, we first summarize the formulation of the non-local energy term E_c^{nl} that enters in a vdW-DF like CX. We next identify the components responsible for capturing non-local interactions in QP states when we use a CX starting point in KI-DFT.

A. Truly nonlocal correlation in CX

The design of the vdW-DFs relies on MBPT characterizations [36, 39–44, 46] of the density-density response function $\chi_\lambda(\mathbf{r}, \mathbf{r}', \omega)$, i.e., the ratio of the density change $\delta n(\mathbf{r})$ that arise when external potential at frequency ω is applied at position \mathbf{r}' . As indicated by the subscript, this response is determined while assuming that the raw inter-electron Coulomb matrix element $V = |\mathbf{r} - \mathbf{r}'|^{-1}$ is scaled by a coupling constant $0 < \lambda < 1$. The adiabatic connection formula (ACF) [38–40, 91],

$$E_{\text{xc}}[n] = - \int_0^1 d\lambda \int_0^\infty \frac{du}{2\pi} \text{Tr} [V\chi_\lambda(iu)] - E_{\text{self}}, \quad (1)$$

is used to convert the formal MBPT input into versions of an XC energy functional of the electron density variation $\rho(\mathbf{r})$. The trace indicate integration with respect to the spatial coordinates of $\chi_\lambda(\mathbf{r}, \mathbf{r}', \omega = iu)$ and V .

The resulting vdW-DF functionals are in practice given by treating the XC design work as an electrodynamics problem [69, 71, 77]. Critical are the focus on collective excitations, compliance with Lindhard screening, and enforcing current conservation and time-reversal symmetry in modeling the local-field response [35, 70, 71]. We start with a generalized-gradient approximation (GGA) for a so-called internal XC function $E_{\text{xc}}^{\text{in}}[\rho]$, comprising the XC terms of the local-density approximation (LDA) [32, 92] and a MBPT-guided choice for the gradient-corrected exchange [70, 72, 93, 94]. This ensures a GGA-type exchange component $E_{\text{x}}^{\text{in}}[\rho]$ in the starting point for the vdW-DF design. We next use an electrodynamics-based recast of the ACF [35, 69, 77] to extract a corresponding initial-guess dielectric function $\epsilon(\mathbf{r}, \mathbf{r}', \omega = iu)$ [72, 93]:

$$E_{\text{xc}}^{\text{in}} = \int \frac{du}{2\pi} \text{Tr} [\ln(\epsilon(iu))] - E_{\text{self}}. \quad (2)$$

This reformulation of the semilocal functional E_{xc}^{in} reflects an exponential resummation, $\epsilon(\omega) \equiv \exp(S_{xc}(\omega))$, of a plasmon-propagator $S_{xc}(\mathbf{r}, \mathbf{r}', \omega)$ that corresponds to the internal GGA [72], so that the initial-guess for the collective excitations (found at $\epsilon(\omega) = 0$) are tracked by logarithmic singularities [71, 95]. Third, we note that the Coulomb Green function G is set up to trace also long-ranged electrodynamics couplings of virtual electron dynamics (for example, as reflected by plasmons) [69, 71] and that the vdW forces are naturally included when we enforce current-conservation, $\epsilon(\omega) \rightarrow \kappa(\omega) \equiv \nabla\epsilon(\omega) \cdot \nabla G$ [69–71, 77]. We therefore use the resulting beyond-GGA recast of the ACF for a formal vdW-DF-method specification [35, 72, 93]

$$E_{xc}^{vdW-DF} = \int \frac{du}{2\pi} \text{Tr} [\ln(\kappa(iu))] - E_{\text{self}}. \quad (3)$$

Finally, we often (but not always [69, 77]) expand the truly nonlocal correlation term

$$E_c^{nl}[\rho] \equiv E_{xc}^{vdW-DF} - E_{xc}^{in}, \quad (4)$$

in terms of both the Lindhard screening and the exponential resummation to second order in $S_{xc}(\omega)$ [35, 70, 72]:

$$E_c^{nl} = \int \frac{du}{2\pi} \text{Tr} \left[S_{xc}^2 - (\nabla S_{xc} \cdot \nabla G)^2 \right]. \quad (5)$$

The complete specification of the CX energy functional [78, 79] is denoted E_{xc}^{CX} . It has an exchange component that mirrors that of E_{xc}^{in} (as far as possible) to ensure XC balance in calculations of energy differences [35, 78]. CX yields a local effective potential that defines the equation of motion for the KS-DFT orbitals. The consistent focus on the plasmon behavior means that the specification of the total correlation, $E_c^{LDA} + E_c^{nl}$, is explicitly given by the density. Using Eq. (5) we can even cast the nonlocal-correlation energy functional [46, 70]

$$E_c^{nl} = \frac{1}{2} \int \int \rho(\mathbf{r}) \Phi_c^{nl}[\rho](\mathbf{r}, \mathbf{r}') \rho(\mathbf{r}') d\mathbf{r} d\mathbf{r}', \quad (6)$$

with a spline representation [96] for what is a universal nonlocal-correlation kernel $\Phi_c^{nl}[\rho]$. This keeps computational costs comparable to that of any GGA-based KS-DFT [96], for example, PBE [45].

In a set of recent designs we have sought to design and leverage generalized-KS vdW-DFs [22, 23, 74, 97–99]. This is done in part to overcome residual accuracy issues in PBE or CX KS-DFT characterizations and sometimes also in the PBE-based range-separated hybrid (RSH), denoted HSE [18–21, 100, 101]; The relevance of having access to global-hybrid RSH vdW-DFs is illustrated and summarized, for example, in Refs. [23, 51, 52, 102, 103]. Starting with two robust vdW-DF versions, CX and rev-vdW-DF2 [104], and replacing, for example, part of the short-ranged GGA exchange, we arrive at two RSH vdW-DFs, denoted AHCX [22] and AHBR [74]. They generalize the HSE by providing a consistent inclusion of truly

nonlocal-correlation effects and, in particular vdW interactions. The AHCX and AHBR are general-purpose options, noting that they are applicable also to metallic systems [22, 74] and for a case when we expect strong static-correlation effects on molecular structure [103]. Still, we can motivate adjustments of these basic RSH vdW-DF designs when used for molecular systems or for semiconductors: For the former (latter) we expect an absence (moderate presence) of asymptotic screening in the exchange descriptions, as implemented in our recent AHBR-mRSH [23] (in global-hybrid vdW-DFs like CX0p [51, 99]). The logic is that the system-specific dielectric function is implicitly set by the Hartree-energy term and should therefore (ideally) also be reflected in the exchange description [16, 19–21, 23, 39, 105]. It is hard to realize this goal in basic XC approximations that aims to be fast and universally applicable [40, 45, 78, 97].

Importantly, practical use of such new hybrid vdW-DFs relies on the orbital-based evaluation of Fock exchange that are now available in QE [22, 81, 106, 107]. That is, our hybrid vdW-DF calculations, e.g., [52, 74, 98, 102, 103], automatically proceed in the generalized-KS framework [97]. This opens for vdW-inclusive QP predictions, when we apply also the ideas so-called optimal tuning [16, 18, 21, 105, 108] to our new molecule-focused AHBR-mRSH [23]. Excitingly, use of AHBR-mRSH with optimal tuning set by consistency, constitute a generalized KS-DFT that complies with the PWL constraint [18, 21, 23, 24, 67] and has high accuracy for both binding energies and QPs of nitrogen-base systems [23].

The present focus on moving also KI-DFT to a vdW-DF start and our introduction of the optimally-tuned AHBR-mRSH supplement each other. The same applies also (to some extent) for the more traditional RSH vdW-DF designs, AHCX and AHBR, and when a Hubbard-U term (U) [109, 110] is added to vdW-DF as the starting XC functional choice [111]. These methods restore PWL [48] to varying extents and, for example, RSH vdW-DFs simultaneously improve parameter-free vdW-DF descriptions of total energies and structure [74]. Also, AHBR-mRSH delivers QP predictions that employ the same nonlocal-correlation description [93] that is already in wide KS-DFT usage [23, 74, 104]. However, by including some Fock exchange in AHBR-mRSH we also simultaneously correct some density-driven errors, e.g, for transition states, that affects the underlying rev-vdW-DF2 functional [23, 74]. In contrast, the here-introduced KI-CX approach (described below) leaves the GS energies and structure unchanged [28, 29] and therefore tests CX directly in terms of both GS and QP properties.

B. CX in Koopmans DFT

From a theoretical perspective, the eigenstates of KS-DFT, obtained using a regular XC functional, provide a reasonable first approximation for studying charge excitations in [10, 11]. Still, while KS-DFT serves us to accu-

rately predict GS properties, its eigenvalues ϵ_i^{KS} and orbitals $\phi_i^{\text{KS}}(\mathbf{r})$ do not directly describe charged excitations such as the set of vertical ionization energies, i.e., the QPs. This is true even though that all the necessary information to describe a frequency moment of the fully interacting spectral function is, in fact, available by simply combining terms of the KS-DFT energy descriptions with also an evaluation of the kinetic-correlation energy [112–114]. Even a PBE-based evaluation of those DFT terms yields a value for the moment of the interacting spectral function that closely reflects a full multi-reference configuration integral studies for small molecules [114].

The limitation of using KS-DFT orbitals as a predictor for QPs arises because KS-DFT relies on using (regular, nonhybrid) XC functionals to define an effective local potential contribution [16, 32] to set the orbital structure. Plotting the total energy as a function of the number of electrons then yields a convex curvature [16]. Use of regular XC functionals to thus directly set KS-DFT orbitals implies a lack of the PWL that is, for example, needed for a DFT-type framework to also satisfy a thermodynamics constraints on charge transfers [16, 67].

Additional information, concealed as MBPT input to the XC functional designs, is needed to also recover accurate results for QP levels [16, 21, 24]. Fortunately the information is still formally retained in the MBPT input and physics logic of good XC designs [114]. By switching to Koopmans-compliant DFT and using the KI-DFT framework with a linear-response extensions of an underlying XC functional (like PBE or the CX version of the vdW-DF method), we can leverage more of the underlying MBPT contents [32, 35, 114] of such robust XC designs also for accurate QP predictions [18, 21, 23, 28, 68, 105].

On a formal level, KI-DFT employs a class of orbital-density-dependent functionals (ODDFs) designed to enforce *generalized PWL*. Specifically, the ODDFs are crafted to enforce that we have a linear energy change with respect to variations in the electron occupation [16, 24, 67]. The CX-based adjustments for KI-DFT, what can also be called the Koopmans functional, is given:

$$E_{\text{xc}}^{\text{KI-CX}}[\rho, \{\rho_i\}] = E_{\text{xc}}^{\text{CX}}[\rho] + \sum_i \alpha_i \Pi_i^{\text{CX}}[\rho, \rho_i]. \quad (7)$$

Here $\{\alpha_i\}$ are screening parameters that account for electronic relaxation effects and ρ_i are orbital-specific density variations $\rho_i(\mathbf{r}) = f_i |\phi_i(\mathbf{r})|^2$; with $0 < f_i < 1$ [24]. We are using the KI form [26, 28, 29, 49] so that the formal KI-functional specification, $E_{\text{xc}}^{\text{KI-CX}}[\rho, \{\rho_i\}]$ reduces exactly to the underlying CX functional form when there is an integer charge in the unit cell (and hence KI-CX does not change KS-DFT structure predictions obtained by CX). However, for partial orbital occupation, the Koopmans-correction term Π_i^{CX} in Eq. (7) restores PWL: It converts the nonlinear dependence of the CX functional on changes in orbital-specific occupations, $\int \rho_i(\mathbf{r}) d\mathbf{r}$, into a linear form between any two integer occupations. This

approach suffices to convert the KS-DFT input (i.e., the choice of the XC) into the KI-DFT tool for making corresponding QP predictions [27, 29, 49]. Further details are provided in Refs. [24, 29].

Conventionally, spectral properties computed via Eq. (7) require minimization of, e.g., the $E_{\text{xc}}^{\text{KI-CX}}[\rho, \{\rho_i\}]$ term, through a two-step nested procedure. The inner loop minimizes the orbital-density-dependent functional contribution, while the outer loop optimizes orbitals in directions orthogonal to the subspace. At convergence one obtain the variational orbitals. These variational orbitals enable computation of $\{\alpha_i\}$ via finite differences. For periodic systems, this parameterization approach requires supercell treatment to eliminate spurious interactions between periodic images.

Although this method rigorously provides both variational orbitals and $\{\alpha_i\}$, its application remains challenging due to the requirement of multiple constrained DFT and Koopmans calculations in supercells for periodic systems. To address this limitation, the KCW formulation, discussed in Refs. [27, 28, 115], employs a second-order Taylor expansion of $\Pi_i[\rho, \rho_i]$ and use of DFPT in primitive cells. This approach assumes coincidence between variational orbitals and maximally localized Wannier functions (MLWFs) $\{w_{\mathbf{k}j}\}$ [116], that are computed by use of the same underlying functional. These MLWFs simplify the minimization of $E_{\text{xc}}^{\text{KI-CX}}[\rho, \{\rho_i\}]$.

To obtain spectral properties within KCW, the resulting total energy $E_{\text{tot}}^{\text{KI-CX}}[\rho]$ is varied with respect to the orbital densities $\rho_i(\mathbf{r})$. This is done by representing it in the Wannier-function basis set

$$\langle w_{\mathbf{k}i} | (\hat{h}^{\text{CX}} + \alpha_{\mathbf{0}i} \mathcal{V}_{\mathbf{0}i}^{\text{CX}}) | w_{\mathbf{k}j} \rangle = \mathcal{H}_{ij}(\mathbf{k}) \quad (8)$$

where $\mathcal{V}_{\mathbf{0}i}^{\text{KI}}$ is the orbital density dependent potential (ODDP) and corresponds to the variation $\delta \sum_j \Pi_j / \delta \rho_i$, and \hat{h}^{CX} is the effective potential defined by CX functional [14]. The subscript index $\mathbf{0}$ in $\mathcal{V}_{\mathbf{0}i}^{\text{CX}}$ and $\alpha_{\mathbf{0}i}$ refers to a decomposition into a set of independent problems, where a supercell calculation with Γ -point sampling corresponds to sampling the folded Brillouin zone of the primitive cell [28]. Hamiltonian diagonalization in Eq. (8),

$$\mathcal{H}_{ij}(\mathbf{k}) \rightarrow \varepsilon_{\mathbf{k}i} \delta_{ij}, \quad (9)$$

yields so-called canonical orbitals that corresponds to the eigenvectors $\tilde{w}_{\mathbf{k}i}$. The eigenvalues of Eq. (9), $\varepsilon_{\mathbf{k}i}$ define the KI-CX (or KI-DFT) predictions for the QP energies. We note that the canonical orbitals have a Block-wavefunction-like character; They are delocalized as they are linear combination of MLWFs $w_{\mathbf{k}i}$. It has been shown that use of an ODDP can provide a QP approximation to the frequency-dependent contraction of the many-body self-energy term [25]. The implication is that ODDFs have the flexibility to accurately describe both total energies and QP excitations.

To elucidate the role of the CX functional in the QP states described by Eq. (8), we note the dependence on

the XC kernel f_{Hxc} , that is, the double derivative of the XC energy functional with density variations. This kernel includes a contributions from the nonlocal-correlation energy functional defined in Eq. (5), specifically, through its second functional derivative:

$$f_c^{\text{nl}}(\mathbf{r}, \mathbf{r}') = \frac{\delta^2 E_c^{\text{nl}}[\rho]}{\delta\rho(\mathbf{r})\delta\rho(\mathbf{r}')}. \quad (10)$$

This linear-response kernel f_c^{nl} depends itself on the electronic density $\rho(\mathbf{r})$. This dependence is in turn explicitly incorporated into the screening parameters $\{\alpha_i\}$, thereby influencing the quasi particle energy solutions.

Appendix A provides details on a formal representation of a plane-wave and grid-based determination of Eq. (10) using the Roman-Soler spline formulation [96] for (the functional nature [46, 70, 71] of) the nonlocal-correlation kernel $\Phi_c^{\text{nl}}[\rho](\mathbf{r}, \mathbf{r}')$ entering Eq. (6). The formal expressions are already coded in the linear-response module (KCW) of QE thanks to a previous study documenting fingerprints of vdW and nonlocal-correlation interactions on phonon predictions [117].

III. COMPUTATIONAL DETAILS

We compute the QP states by the KOOPMANS-DFT code package [29, 30], using the KI-DFT versions, and the above-summarized KCW formulation [28]. All those calculations as well corresponding KS-DFT studies are done using norm-conserving PBE-type (scalar-relativistic) pseudopotentials from the PseudoDojo library [118]. That is, we employ dual projectors and generalized norm conservation to accurately reproduce all-electron potential binding and scattering properties. Appendix B presents a discussion of numerical stability for the QP-energy predictions with the wavefunction energy cut off $E_{\text{cut}}^{\text{wf}}$ (and, for the strictly two-dimensional BN1 system, the height c of the modeling cell). This analysis leads us to use $E_{\text{cut}}^{\text{wf}} = 200$ Ry (400 Ry) for bulk (single-sheet) h-BN, while doubling the grid for the density variations; Exceptions are explicitly stated.

The workflow for KI-DFT QP studies can be summarized in the following steps:

1. Do a MLWFs ($|w_{\mathbf{k}i}\rangle$) for the KS states.
2. Convert the $\{|w_{\mathbf{k}i}\rangle\}$ to Wannier orbital densities $\{w_{\mathbf{k}i}^* w_{\mathbf{k}'i}\}$
3. Calculation of $\{\alpha_{\mathbf{k}i}\}$ via DFPT.
4. Diagonalize the Hamiltonian in Eq. (8) to obtain $\{\tilde{w}_{\mathbf{k}i}\}$ and $\{\varepsilon_{\mathbf{k}i}\}$

In the initial step, KOOPMANS code executes the QE codes PW.X and PH.X. Subsequently, the MLWF algorithm is carried out through PW2WANNIER90.X and WANNIER90.X [119]. Steps two through four employ the KCW.X code that also gave the workflow naming [28].

The QP band structure calculations is given by Eqs. (7) and (8); The orbital resulting in KI-CX results are themselves the KI-CX QP predictions. These results are compared to QP states of KI-PBE and the KS states of the corresponding underlying functionals CX and PBE. KI-PBE calculations are standard in the KOOPMANS-DFT code. To do band structure calculations with KI-CX it is necessary to explicitly introduce a selection of the CX functional in the ‘QE’ specification, see tutorial Ref. [30].

We compute QP states KI-CX (technically, ‘Koopmans DFPT’ [28] with a CX start) for the h-BN monolayer (BN1) and for bulk h-BN in the experimentally observed AB and AA’ stacking configurations. The structural characters of these h-BN systems are illustrated in Fig. 1 that also identifies the set of relevant high-symmetry k -points in the Brillouin zone (BZ).

The BN1 structure (first column) is a monolayer exhibiting the conventional *honeycomb* lattice, where boron (green) and nitrogen (gray) atoms with valence 3 occupy alternating vertices of the hexagonal network. In-plane sp^2 bonding between boron and nitrogen atoms provides structural stability and rigidity for this single-sheet system. The choice of in-plane lattice constants for the BN1 system is set by an early experimental structure characterizations of h-BN [120]: For BN1 we use an hexagonal unit cell with in-plane parameters $a = b = 2.504$ Å and a $7 \times 7 \times 1$ k -point grid sampling. In our periodic modeling used for QE studies we set $c = 20$ Å; This choice gives sufficient distance between repeated images of the BN1 layer that we can, in practice, ignore spurious inter-layer forces in characterizations of cohesion as well as of QP energies, as discussed in Appendix B.

Bulk AB stacking (second column of Fig. 1) features a graphite-like staggered arrangement of hexagons, where half of the atoms (for example, all of the nitrogens) sit directly on top of a different type of atom in the neighboring layer. For our calculation study we use a $7 \times 7 \times 3$ k -point grid with lattice constants set at an average over measurements on what are interpret [121] as experimentally characterized AB structures, $a = b = 2.505$ Å and $c = 6.661$ Å.

The third column of panels in Fig. 1 show schematics of the AA’ form that is the ground-state of h-BN. Contrary to the AB form, the ground-state configuration stacks the BN layers so that all of the boron (nitrogen) atoms in a given layer sit directly on top of a nitrogen (boron) atom in neighboring layers. For our AA’ studies, we use an hexagonal unit cell with lattice constants parameters $a = b = 2.504$ Å and $c = 6.66$ Å that represent averages of values extracted by experiments [120–122]. Also, we again use a $7 \times 7 \times 3$ k -point sampling.

Additionally, we include a study demonstrating the full vdW impact on the QP band structure, contrasting what we call consistent-KI-CX and consistent-KI-PBE descriptions. That is, we track not only the *direct* changes arising when we switch from a PBE to a CX starting point in KI-DFT at the same fixed geometry, but also the *additional indirect signatures* that arise because a

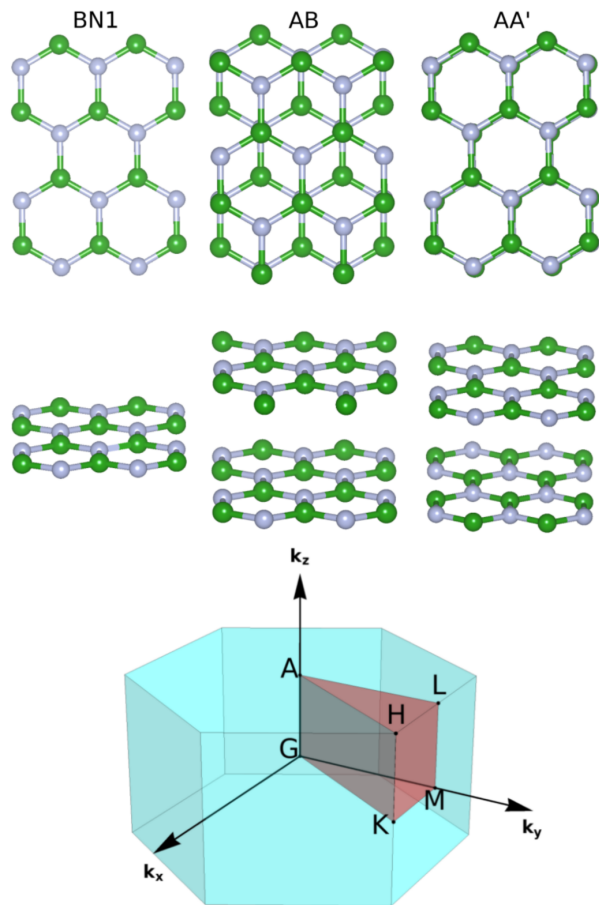


FIG. 1. Atomic as well as Brillouin-zone structure of h-BN structures in the single-sheet form, denoted BN1, and in the two stable bulk forms, AB and AA. The panels of the first and second row show the atomic structures as shown from a perspective perpendicular and parallel to the slide plane. The bottom panel shows the Brillouin zone (BZ) of the bulk h-BN forms in blue and the reduced BZ zone in red. This panel also identifies the set of high-symmetry k -points of the reduced BZ as relevant for these hexagonal systems.

GGA PBE is not set up to accurately characterize the bulk h-BN structure [35, 123, 124]. The importance of this is discussed in the following section IV. In practice, we complete KI-PBE and KI-CX QP characterizations, having first relaxed the interlayer distance of the AA' system using KS-DFT with the PBE and the CX functionals, respectively. Specifically, we find that CX-based and PBE-based structure optimizations yield lattice constants $c = 6.448 \text{ \AA}$ and $c = 8.560 \text{ \AA}$, respectively. The former and latter structure is then used in ensuing KI-CX(CX) and KI-PBE(PBE) QP characterizations.

For the three materials forms at experimental structures, and for the demonstration of indirect vdW fingerprints, we presents analysis of the resulting QP bandstructures, using a shared computational treatment. The Gygi-Baldereschi method [125] is used to address the $\mathbf{q} \rightarrow 0$ divergence of the Coulomb interaction in our peri-

TABLE I. Projections for the iterated MLWF determination.

Site	Angular momentum $\Theta(\theta, \phi)$	Radial functions
Occupied bands		
N	s	$R_2(r)$
N	p_x, p_y, p_z	$R_2(r)$
Virtual bands		
B	p_z	$R_2(r)$

odic systems, both in the initial QE code stages and when setting the screening coefficients α_i for the KI-DFT studies, above. The Gygi-Balderashi approach assumes some level of isotropy and its use is more motivated for the bulk BN cases than for the single-sheet BN1 system.

As highlighted in Eq. (8), Wannier functions serve as the initial basis for our set of KOOPMANS DFPT studies. That is, we use MLWFs to generate localized orbitals $\{|w_{\mathbf{R}i}\}$ and we find a set of initial Wannier functions that work for the layered h-BN systems. These initial Wannier functions are selected using an initial projected density of states (PDOS) that we obtain via use of the QE PROJWFC.X code. They take the form of modified spherical harmonics, with details listed in Table I.

The occupied bands are located at the nitrogen atoms in the unit cell, with the following angular momentum shapes s and p_x, p_y , and p_z and each of these having a radial function $R_2(r)$. For the virtual states we chose p_z but now located at the boron atoms, with the radial functions $R_2(r)$. This process is verified by the convergence of the MLWF algorithm. We have also tried to use hybrid sp^2 orbitals instead but they did not converge in the MLWF procedure, even though suggested by chemical intuition.

Beyond initial Wannier-function selection, we must disentangle virtual bands from occupied states to construct well-localized Wannier functions. The disentanglement window spans from the Kohn-Sham highest occupied molecular orbital (HOMO) to `dis_win_max`, which defines the upper energy bound for disentanglement. Simultaneously, `dis_froz_max` sets the upper limit of the frozen energy window. The layered bulk systems AA' and AB we employ parameter values of `dis_froz_max = 0.6 eV` and `dis_win_max = 16.0 eV`. For the monolayer BN1 system, we adjust these parameters to `dis_froz_max = 0.5 eV` and `dis_win_max = 14.0 eV`.

In contrasting predictions of the KI-DFT predictions and KS-DFT approximations for the QP bandstructures we face, in principle, a problem of how to pick a reference energy. Bandstructure characterizations are often reported with QP energies listed relative to the valence band maximum (VBM) but such values are generally affected by both the atom configurations and choice of methodology. Ideally, as the QPs reflect vertical excitations, we would like to list the variation with QP energies defined relative to the true vacuum. However, in a planewave code like QE, we can only get orbital-energy values relative to what is the average electrostatic potential in a given cell, with a given atomic configuration (and

choice of pseudopotentials) and for the electron-density variation that is produced in the given DFT method and given choice of XC functional [126].

Nevertheless, in predictions and discussions of the QP bandstructure differences *at fixed experimental structures*, it is possible and motivated to define a common reference. Specifically, in Figs. 2 and 3 we have shifted all the bands using

$$\sum_{\mathbf{k},i} \varepsilon_{\mathbf{k}i}^{IM} = \sum_{\mathbf{k},i} \varepsilon_{\mathbf{k}i}^M - \varepsilon_{\text{VBM}}^{\text{KI-CX}} \quad (11)$$

where $\varepsilon_{\text{VBM}}^{\text{KI-CX}}$ the VBM of KI-CX and where M corresponds to difference choices of the methodologies: PBE, CX, KI-PBE and KI-CX. The point is that since the atomic and cell geometry are shared (and we use the same pseudopotentials in all studies) the average electrostatic potential can only vary because of differences in the electron-density variation. However, PBE and CX are both widely tested and both documented to provide highly accurate accounts of the electron-density variations (at fixed structure) that must therefore be almost identical in the case of PBE and CX studies. Furthermore, by design of the KI-DFT method, it is also so that the KI-CX and CX yields exactly the same electron density variations (at shared geometries) and the same applies for KI-PBE and PBE [29]. By the explicit procedure that the QE code uses to set the average electrostatic potentials, Refs. [126, 127], no differences can therefore arise for the electrostatic reference energy in KI-CX and CX. The *same offset* brings the here-reported bandstructures in alignment with a QP bandstructure mapping that reflects the true vacuum level.

IV. RESULTS AND DISCUSSION

Unlike graphite, h-BN experimentally demonstrates five distinct stacking arrangements, with only two being thermodynamically stable and the remaining three metastable [128, 129]. A key factor driving interest in h-BN is its wide band gap, which is systematically underestimated in KS-DFT [129]. In contrast, GW approximations align more closely with experimental observations [130]. Here we seek to compute and contrast QP band structure results of the stable h-BN forms AA'-stacked, AB-stacked, and monolayer h-BN (BN1), Fig. 1.

Our study and analysis highlight changes arising as we move from KS-DFT to KI-DFT and as we include (in KI-CX) nonlocal-correlation effects. In particular, we track differences (i) between use of semi-local and truly nonlocal-correlations in KS-DFT (PBE vs. CX results); (ii) between use of a semi-local functional for KS-DFT and for its KI-DFT counterpart (PBE vs. KI-PBE); (iii) between use of a vdW-DF for KS-DFT and for the corresponding KI-DFT (CX vs. KI-CX); and finally, (iv) arising when we include truly nonlocal-correlations in KI-DFT (comparing KI-CX and KI-PBE results).

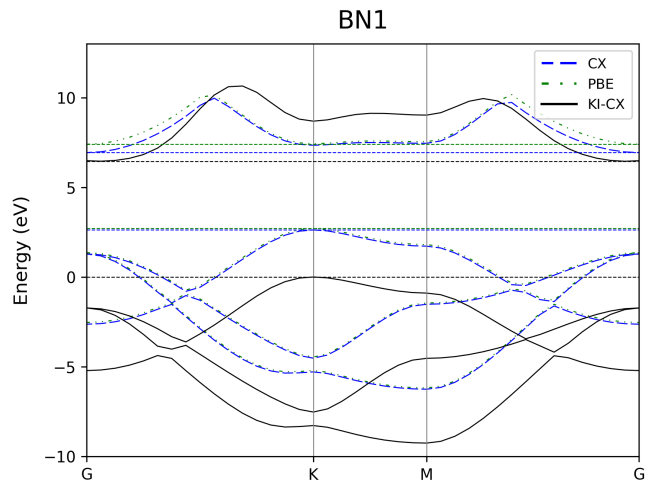


FIG. 2. Comparison of BN1 QP band-structure predictions, as evaluated in PBE, CX and in KI-CX in a $c = 20$ Å cell to minimize the impact of spurious couplings between repeated images in our plane-wave-DFT studies. The top of the KI-CX QP-valence band is used as a shared reference energy, as motivated in the text.

A. Bandstructure results and analysis

In Figs. 2 and 3 we show comparisons of the band structure predictions obtained at experimental structures by our set of methodologies.

Figure 2 summarizes our results for the single-sheet BN1 case (at an experimentally relevant atomic in-plane geometry). Here we trace out the QP dispersion along a k -point path defined by the string ‘GKMG’ of high-symmetry points that are relevant for a two-dimensional hexagonal system, see bottom panel of Fig. 1.

Figure 3 presents our bandstructure predictions obtained for the two h-BN bulk systems (AB and AA’). There we trace out the QP-energy variation along a richer path, ‘GKMGHLLA’, of the high-symmetry k -points that are relevant for such bulk hexagonal systems, see again the bottom panel of Fig. 1. The panels in the first (second) column of Fig. 3, report our results for bulk h-BN in the AB (AA’) form. The first row of panels presents comparisons of the QP bandstructure approximations defined by KS orbitals and obtained in PBE and CX, for the two bulk structures. The third (second) row of panels contrasts QP predictions as provided by CX and KI-CX (by PBE and KI-PBE) studies. The last row of panels reports comparisons of KI-PBE and KI-CX QP predictions, again for the two bulk h-BN forms.

We note in passing, that we are not showing the internal (2s) first bands in any of our band structure mappings. This is done to present a clearer view of what is happening near the valence and conduction band edges.

In the following discussion of the band structures, we will use subscripts at symmetry points to denote the valence- and conduction-bands that define various (gen-

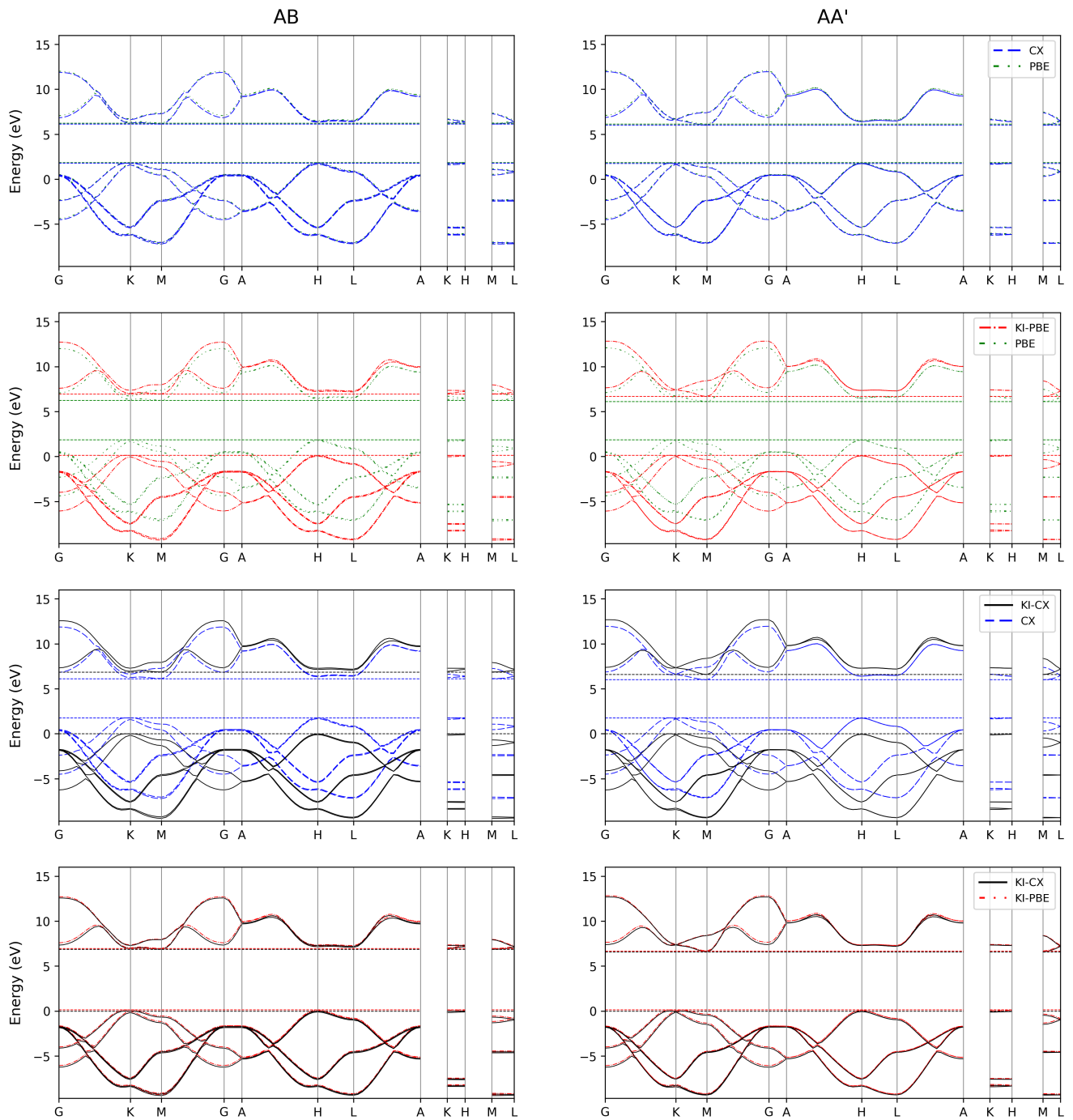


FIG. 3. Band structure comparison for h-BN structures AB and AA', with KI-PBE and KI-CX results provided in KI-DFT and PBE and CX results in KS-DFT, i.e., using the same underlying CX functionals.

erally indirect) gaps of potential key interband transitions. For example, K_c indicates the conduction band at the K point, while K_v denotes the valence band at the same symmetry point. The set of key (potential) interband transitions are identified by the start and end points, e.g., $K_v \rightarrow K_c$, when we summarize and discuss our set of QP predictions across the structures.

1. BN1

In Fig. 2 we compare PBE, CX and KI-CX results for the QP band structure in the monolayer BN1 system, here in the standard set up using a $c = 20 \text{ \AA}$ cell height for the computational modeling. Table II provides a compilation of our quantitative results for gaps defined by valence-to-conduction-band transitions among the set

Method	$G_v \rightarrow G_c$	$M_v \rightarrow M_c$	$K_v \rightarrow G_c$	$K_v \rightarrow K_c$	$M_v \rightarrow G_c$	$K_v \rightarrow M_c$	Fundamental Gap
PBE	6.04	5.74	4.69	4.71	5.59	4.83	4.69 ^a
CX	5.65	5.74	4.31	4.72	5.22	4.83	4.31
KI-CX ^b	8.21	9.92	6.48	8.69	7.38	9.02	6.48
KI-CX ^c	8.20	9.99	6.47	8.72	7.37	9.09	6.47
GW_0^d	-	-	7.43	7.90	-	8.00	7.43

^a Nearly degenerate.

^b Computed at $c = 20$ Å, at $E_{\text{cut}}^{\text{wf}} = 400$ [Ry].

^c Computed at $c = 30$ Å, at $E_{\text{cut}}^{\text{wf}} = 400$ [Ry].

^d Ref. 76.

TABLE II. QP-gap energies (in eV) by PBE, CX, and KI-CX for valence-to-conduction-band transitions at different symmetry points for the single-sheet h-BN structure BN1, with comparison to literature GW_0 results.

of high-symmetry k -points. We note that we could not complete a corresponding KI-PBE study because the KI-DFT computational scheme fails to converge the screening parameters that enter in the KI-PBE functional for conduction-band QPs.

Contrasting the KS-DFT descriptions by PBE and CX, we observe a small (a fraction of an eV) rigid downward shift for the valence bands in CX relative to PBE. In the conduction band, CX shifts states downwards occurring at G_c , resulting in a slightly reduced band gap. In both cases, the VBM resides at the K_v symmetry point. The crucial difference lies in the conduction band minima (CBM): PBE finds the CBM as essentially degenerate between K_c and G_c , predicting a minimum direct quasi-particle band gap (QP-gap) $K_v \rightarrow K_c$ of 4.71 eV and minimum indirect gap $K_v \rightarrow G_c$ of 4.69 eV. In contrast, CX clearly indicates the indirect transition $K_v \rightarrow G_c$ as the fundamental gap at 4.31 eV (compared to 4.72 eV for $K_v \rightarrow K_c$), in qualitative agreement with GW_0 results, see Table II.

Comparison of KI-CX with CX results reveals an essentially rigid downward shift of about 2.5 eV in the KI-CX valence bands. For the conduction band we see that KI-CX lowers the G_c QP energy, while M_c and K_c QP energies are shifted upwards. As a consequence, we find that use of KI-CX as a QP predictor does provide an adjustments of the underestimated PBE and CX gaps.

The left panel of Fig. 4 shows a plot of the QP wavefunction as obtained by KI-CX for the conduction-band at the high-symmetry Γ point ‘G’. This variation is shown for reference. It allows us to illustrate and discuss some of the impacts that the interlayer vdW attraction has on the details of bulk-AB and bulk-AA’ QPs, next.

2. AB

In the first column of Fig. 3 (identified by an ‘AB’ header), we show comparisons of the QP dispersion relations for bulk h-BN in the AB structure. The top section of Table III shows a numerical comparison of the gap predictions that we extract for the set of valence-to-conduction QP band gaps.

In the first row of the AB column of Fig. 3, contrast-

ing PBE and CX results, we observe that the valence bands are nearly identical by either of these KS-DFT descriptions. There is merely a small shift of ≈ 0.01 eV downward in CX near G_c . The VBM is located at H_v . The indirect QP-gap reflects a transition $H_v \rightarrow M_c$ at 4.39 eV and 4.36 eV for PBE and CX, correspondingly.

The second-row panel of AB results shows the comparison of PBE and KI-PBE. The occupied bands of KI-PBE are down-shifted relative to PBE, while the unoccupied bands are shifted higher in energy in KI-PBE. In KI-PBE, the fundamental band gap is indirect and corresponds to the transition $T_v \rightarrow M_c$ at 6.83 eV. Here T_v is a non-symmetric k point that lies on the path from G_v to K_v , being close to K_v . This AB-system VBM corresponds (as a shifted K_v point) to that which was previously predicted for the AA’ system by use of HSE+D3 [75, 101, 132]. We also observe that degeneracy of the unoccupied bands breaks between $A_c - H_c$ and $L_c - A_c$ in the KI-PBE description.

In the third-row panel, comparing KI-CX and CX results, we find that use of KI-CX again produces an overall downshifting of the valence-type QP bands while in the conduction bands we observe some differences. Like for KI-PBE, in the upper part of the Brillouin-zone hexagon (spanned by high-symmetry points A-H-L-A, figure 1), we observe a breaking of the degeneracy between $A_c - H_c$ and $L_c - A_c$. The results of the second- and third-row panels, taken together, suggest that the use of KI-DFT and the enforcement of PWL (rather than the choice of underlying functional) is responsible for breaking the degeneracy. KI-CX predicts the $T_v \rightarrow M_c$ transition as the fundamental gap, at 6.87 eV.

In the last-row panel of AB results, we compare the Koopmans methods directly and find that use of KI-CX gives predictions for valence and conduction bands that primarily causes a small downward shift, largest around G_c . For the conduction bands, between $A_c - H_c$ and $L_c - A_c$, we also observe a slightly smaller separation between the bands in KI-CX near A_c .

The second panel of Fig. 4 shows the canonical orbital density predicted by KI-CX at the CBM. Contrasting with the corresponding BN1 panel, we find that there is now a different p_z -orbital character reflecting orbital overlaps midway between the layers. For the small σ -

Method	$G_v \rightarrow G_c$	$M_v \rightarrow M_c$	$K_v \rightarrow G_c$	$K_v \rightarrow K_c$	$M_v \rightarrow G_c$	$K_v \rightarrow M_c$	Fundamental Gap
AB							
PBE	6.53	5.10	5.22	4.51	5.91	4.41	4.39 ^a
CX	6.36	5.07	5.07	4.49	5.76	4.38	4.36 ^a
KI-PBE	9.23	7.52	7.48	6.92	8.14	6.86	6.83 ^b
KI-CX	9.06	7.56	7.36	6.96	8.01	6.90	6.87 ^b
HSE+D3 ^c	-	-	-	6.23	-	-	6.02 ^b
AA'							
PBE	6.58	4.75	5.35	4.95	5.71	4.39	4.28 ^b
CX	6.41	4.71	5.20	4.96	5.55	4.36	4.24 ^b
KI-PBE	9.30	7.02	7.62	7.39	7.97	6.67	6.54 ^b
KI-CX	9.14	7.06	7.50	7.46	7.85	6.71	6.58 ^b
KI-CX(CX)	8.65	6.88	7.06	7.49	7.30	6.64	6.47 ^b
GW^c	8.40	6.50	6.90	6.90	7.30	-	5.95 ^b
Exper. ^d	-	-	-	-	-	-	6.08

^a Corresponds to $H_v \rightarrow M_c$
^b Corresponds to $T_v \rightarrow M_c$
^c Ref. 76.
^d Ref. 131.

TABLE III. QP gap predictions (in eV) for valence-to-conduction-band transitions in h-BN bulk structures AB, and AA'. Our results computed in the Koopmans-corrected functionals KI-PBE and KI-CX, as well as in the underlying KS-DFT functionals PBE and CX, are compared to literature GW values and experiment, where available.

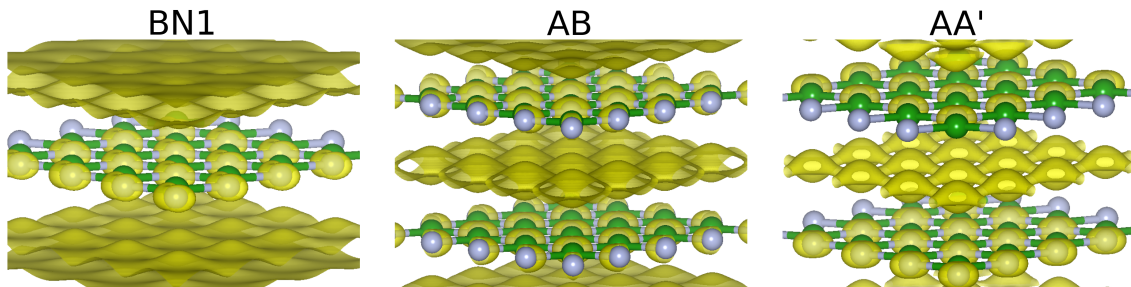


FIG. 4. Real-space canonical orbital densities $|\langle \mathbf{r} | \tilde{w}_{\mathbf{R}_i} \rangle|^2$ at the CBM for h-BN structures BN1, AB, and AA', computed using Koopmans-DFT as KI-CX. The iso-surface constant for BN1 is 5 meV and for AB and AA' corresponds to 7 meV.

orbital signature of the VBMs, centered on the nitrogen atoms, there are also differences. These VBM changes arise because the vdW forces provide interlayer attraction to shorten the interlayer separation from essentially decoupled to the experimental value that characterizes our AB study [69, 72, 74, 123]. As such, the QP CBM changes represent vdW signatures but they should be seen as indirect [124], set exclusively by the structural change. In fact, use of the KI-CX and KI-PBE (not shown in Fig. 4) at the experimental structure yields almost identical details in QP CBM orbital densities.

3. AA'

The last column of panels of Fig. 3 reports our predictions for the QP bandstructure of the AA' system, as described in our set of functionals and DFT frameworks. The bottom section of Table III provides a comparison of

our numerical results for the set of high-symmetry band gaps among the methods and with literature GW characterizations and experiment.

In the first-row panel of AA' results in Fig. 3, we find a similar behavior as in the AB system. The PBE and CX results show no significant differences beyond a small displacement of valence bands, but some changes emerge for the virtual bands. The fundamental gaps emerging in PBE and CX studies reflect again an indirect $T_v \rightarrow M_c$ transition [75], at 4.28 eV and 4.24 eV, respectively. We find that the VBM is at the same non-symmetric k point T_v for the AA' system as for the AB system.

In the second-row panel of AA' results, contrasting PBE and KI-PBE, we observe characteristics similar to those arising for the AB structure. The main difference from the AB case is that here KI-PBE reduces the gap by lowering the energy at the symmetry point M_c . KI-PBE predicts the fundamental-gap QP transition as $T_v \rightarrow M_c$, at 6.54 eV.

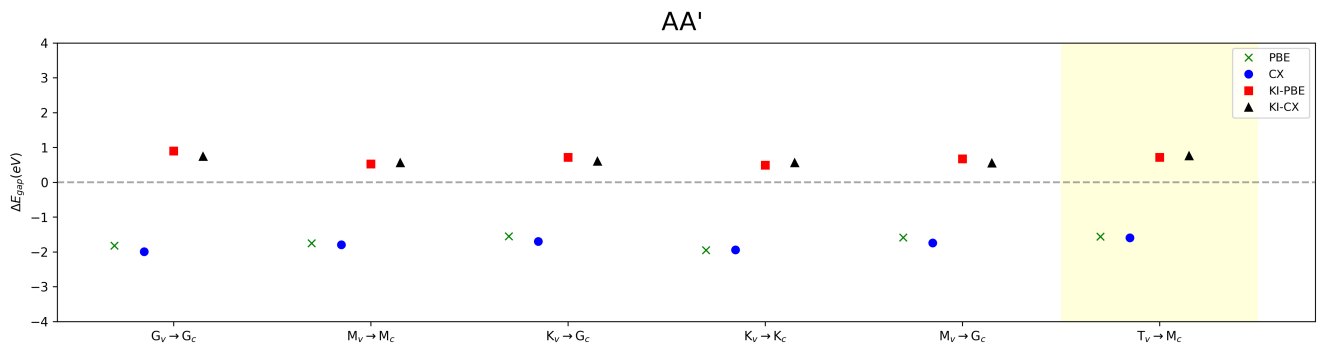


FIG. 5. Deviations with respect to GW of our set of predictions for QP-transitions between the indicated set of high-symmetry k -points for AA' . We highlight the performance comparison at the fundamental gap, that is, for the QP transition that corresponds to having the smallest valence-conduction-band QP energy separation.

In the third-row panel, we contrast CX and KI-CX predictions for the QP band structure. As a Koopmans functional, KI-CX predicts what mostly amounts to an overall lowering of the occupied (valence-type) QP energies, relative to the CX description. However, we find that along the path from M_v to G_v , the band crossing occurs closer to G_v in KI-CX than for CX. A similar shift of band crossing is also evident between L_v and A_v .

Meanwhile, for the conduction-type QP states (unoccupied orbitals), we find that along the full path from G_c to A_c , the use of KI-CX produces a general shift (as does KI-PBE), resembling what is documented above for the AB system. Nevertheless, the switch from CX to KI-CX also causes an enhanced lowering of the conduction-type QP energies close to M_c . The KI-CX predicts (like KI-PBE) the transition $T_v \rightarrow M_c$ [75] as the fundamental gap, now at 6.58 eV.

Finally, we compare the two KI-DFT descriptions of the QP bandstructure in the last-row panel of AA' results. We find for the occupied orbitals that use of KI-CX slightly shifts the bands downward while otherwise maintaining a close similarity to KI-PBE results. Both functionals locate the VBM at T_v . Again, both methods predict that the fundamental gap corresponds to a QP transition $T_v \rightarrow M_c$, Table III.

Nevertheless that are some differences. In the upper Brillouin-zone region (tracing the set of ‘A-H-L-A’ high-symmetry k points of the BZ), we observe that KI-CX predicts a small but systematic and visible lowering of QP energies compared with KI-PBE. The overall lowering is expected since the reference value of the potential (by which we measure QP energy positions) is affected by the actual electron-density variation $\rho(\mathbf{r})$. While the CX and PBE densities are indeed so close that CX and PBE provide nearly identical workfunction predictions for transition metals [35], there are small differences in the $\rho(\mathbf{r})$ profiles that we compute in CX (and hence in KI-CX) and in PBE (and hence in KI-PBE).

The third panel of Fig. 4 identifies again signatures of the vdW interlayer attraction on the variation of the QP-CBM density evaluated at the M_c point. As for the AB

structure, the KI-CX predictions for the CMB is a QP orbital which exhibits lobes with p_z and π -bond characters that resemble those found for the AB structure. However, our KI-CX QP characterization for AA' shows that the corresponding CBM orbital density exhibits a modulation, it has periodically voids in the regions between the h-BN layers. These voids are found at positions that correspond to the centers of the h-BN-atom rings. In effect, we find that the CBM QP is trapped along bonds between the hexagonal network of boron and nitrogen atoms. Accordingly, there are also differences at the in-layer σ -bond positions.

Again we interpret these vdW-binding signatures as indirect QP effects because we find essentially no difference in behavior in the KI-PBE characterization of the AA' system (not shown). We repeat that the PBE lacks an account of vdW and other truly nonlocal correlation effects [35] and that KI-PBE cannot provide a full characterization of the QP signatures in bulk h-BN. The alignment of KI-CX and KI-PBE characterizations of QPs discussed so far only results because we consider bulk systems with the layer separations fixed at experimentally observed values. We shall return to more detailed arguments for seeing changes in the QP CBM spatial variation relative to the BN1 case, Fig. 4, as indirect vdW signatures.

B. Comparison with MBPT

Accuracy for BN1 QPs. Table II presents an overview of the quantitative results we find in the KI-CX characterization for BN1. We observe that both PBE and CX give gaps that are consistently smaller than those found in GW_0 [76]. While minimal differences exist between these functionals, PBE does yield a better agreement for the BN1 fundamental gap, at the $K_v \rightarrow G_c$ transition, while CX is in closer qualitative agreement with GW_0 in that it lifts the PBE near-degeneracy with the gap for the $K_v \rightarrow K_c$ transition. The descriptions of the QP energies can be seen as clearly improved in KI-CX.

Appendix B summarizes some challenges that we face

in numerically converging these KI-CX results with respect to modeling parameters for BN1, for example, forcing us to use a higher $E_{\text{cut}}^{\text{wf}}$ for the conduction-band QP energies than what is required to converge the KS-DFT/KI-DFT total-energy description (or valence-band QP energies). We expect this numerical challenge arises, in part, because the screening assumption [125] that we presently need to use is not naturally set up to handle strictly two-dimensional problems. That is, future KI-CX (or KI-PBE) studies, using a better screening handling for two-dimensional systems [133], may permit computationally cheaper QP descriptions.

Accuracy for AA' QPs. Table III presents an overview of the accuracy that exists in PBE, CX, KI-PBE, and KI-CX predictions for the QP energies of bulk h-BN, our main focus. The assessments are made in terms of band gaps, that is, energy differences between QP transitions at the set of k points that correspond to local extrema in the QP band structure. Specifically, we make quantitative comparisons of QP predictions for these band gaps by comparing with literature GW results that exist for the bulk AA' structure [76]. We note in passing that the GW value for the AA'-system fundamental gap is in close agreement with an experimental observation [131], see Table III. We also note that our screening approximation [125] is motivated for bulk systems and that we found these calculations robust already when picking the same $E_{\text{cut}}^{\text{w}} = 200$ Ry value that suffices for the total-energy description, as discussed in Appendix B.

Figure 5 presents an overview of method performance, as revealed by accuracy on the description compared with GW results that we take as references. The figure focus on the gaps of the AA' system and we mirror the result organization used in Fig. 1. That is, we use identical color coding for the respective KS-DFT and KI-DFT results, summarizing the method performance in terms of the deviation:

$$\Delta E_{\text{gap}}^{\alpha,\beta} = \delta\varepsilon^{\alpha} - \delta\varepsilon^{\beta}, \quad (12)$$

$$\delta\varepsilon^{\alpha/\beta} = \varepsilon_{\text{DFT}}^{\alpha/\beta} - \varepsilon_{\text{GW}}^{\alpha/\beta}. \quad (13)$$

Here $\varepsilon_{\text{DFT}}^{\alpha}$ ($\varepsilon_{\text{DFT}}^{\beta}$) identifies the QP-energy prediction at a given high-symmetry point of the conduction band (valence band) as described in PBE, CX, KI-PBE, or KI-CX, while $\varepsilon_{\text{GW}}^{\alpha/\beta}$ represents the corresponding reference value. The gray horizontal dashed line (at zero deviation) permits an easy comparison among different types of QP gaps. Color shading highlights the deviation that corresponds to the fundamental QP gap, as consistently determined in KI-DFT and GW for the AA' system.

Figure 5 shows that use of a KS-DFT approach (in CX and PBE) persistently leads to an underestimation of the gaps for QP transitions. Use of the corresponding KI-DFT forms leads instead to small overestimation of gaps and significant reductions in the absolute deviation values. That is, PBE and CX are both good starting points for a KI-DFT characterization of QPs overall, when investigating structures fixed at their experimental

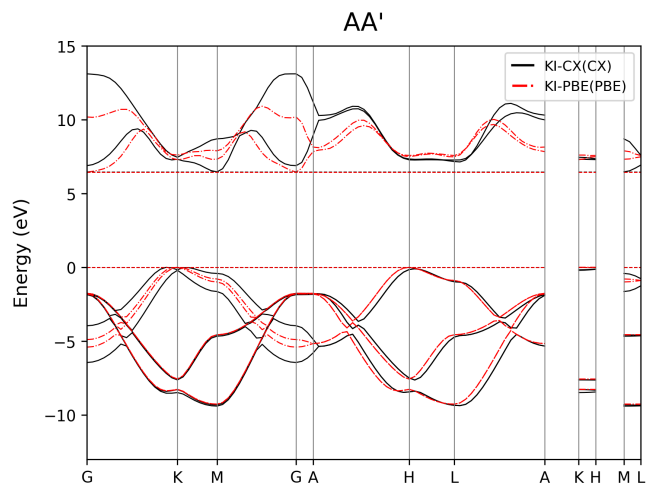


FIG. 6. Comparison of QP predicted for AA' by KI-CX(CX) and KI-PBE(PBE). Here the KI-CX(CX) QP predictor results when we use KI-CX at the atomic configuration predicted by a CX-based KS-DFT structure optimization; KI-PBE(PBE) results instead when we systematically stick to PBE in the modeling procedure. As the atomic structures differs, we shift the pair of resulting KI-DFT bandstructures differently, i.e., by their respective (functional-specific) predictions for the VBM-energy values.

geometry.

We observe that, for the transitions $G_v \rightarrow G_c$, $K_v \rightarrow G_c$, and $M_v \rightarrow G_c$, the KI-CX predictions are closer to GW , while for the rest of the transitions, KI-PBE are slightly closer to GW . Both methods for KI-DFT give predictions for band gaps (originating at the set of relevant conduction- and valence-band extrema) that remain within 1 eV from corresponding GW results, taking the form of a near-constant offset. The latter observation suggests that both KI-PBE and KI-CX give an accurate treatment of transitions involving the conduction band G_c symmetry point for bulk systems.

C. Fingerprints of vdW: QP bandstructures at CX- and PBE-predicted atomic structures

We finally provide analysis that substantiates our interpretation of all so-far discussed major QP changes as indirect vdW-type (or nonlocal-correlation) signatures. Our discussion leads us to identify additional such signatures on the here-predicted QP nature for bulk h-BN.

We first define general vdW fingerprints on the QP bandstructure and recall the logic of sorting these into what we call direct and indirect features, for example, as discussed in Ref. 124. We note that proximity of interacting fragments (in our case h-BN layers) impacts the nature [35, 113] as well as the scaling and strength of vdW forces [134, 135]. We expect stronger vdW signatures to appear also in the QPs bandstructure [124] as the interlayer separation shortens, something that the inclu-

sions of the vdW-DF E_c^{nl} term itself drives. Use of CX in KI-DFT as well as in a KS-DFT structure optimization means that we 1) include vdW attraction between the layers and thus correct for the large (interlayer) under-binding that exists in a GGA like PBE [69, 74, 123] and, in turn, that we 2) provide a *consistent-KI-CX* QP characterization, covering vdW impacts to the extent that they are included in CX. The correspondingly defined ‘KI-PBE(PBE)’ approach should only be used as a reference for discussions when vdW forces are important.

By contrasting results for AA’ by KI-CX(CX) and KI-PBE(PBE), below, with those of the fixed-structure KI-CX and KI-PBE method, above, we arrive at a precise definition of direct and indirect vdW fingerprints in QP predictions. KI-CX(CX) versus KI-PBE(PBE) differences are nominally a full description of vdW and other truly nonlocal-correlation fingerprints on the QP nature. The same holds in practice for differences between KI-CX(CX) results for AA’ and KI-CX characterizations of BN1 (because a switch from PBE to CX has little effect on the description of intralayer bonding). Meanwhile, KI-CX versus KI-PBE differences are denoted as ‘direct’ vdW band-structure impacts because they reflect the same atom configuration and track the impact of introducing the truly nonlocal correlation term E_c for what is, in practice, nearly identical electron-density variations $\rho(\mathbf{r})$; The similarity of CX and PBE predictions for $\rho(\mathbf{r})$ at a fixed structure has been validated by comparing workfunction shifts and vibrations across many types of systems [35, 51, 102]. We identify ‘indirect vdW signatures’ on our QP predictions, when KI-CX(CX) versus KI-PBE(PBE) differences cannot be identified as a direct vdW fingerprint.

Before turning to specific interpretations, we express a general expectation that indirect vdW effects on QPs will be dominant for layered systems [124]. This follows because PBE and hence KI-PBE(PBE) cannot drive a layered bulk system to any meaningful interlayer proximity as discussed both previously [69, 123] and as computed here: It is alone our CX prediction of structure that is close to the experimental characterizations of h-BN, see Section III. In any case, having the capability, via KI-CX(CX) studies, to predict both indirect and full vdW effects, is essential when we seek to predict QPs either independently from an existing experimental structure characterization [3], or in the absence of sufficient structure data [102, 103, 124, 136], or even ahead of actual material synthesis [124, 137].

Figure 6 reports our comparison of the QP bandstructure predicted in KI-CX(CX), solid black line, and in KI-PBE(PBE), red dashed-dotted line. As stated in the previous sections, for these QP predictions we now employ what we can call native interlayer distances. That is, we set c lattice constant for the AA’ system by a CX-based structure optimization (giving $c = 6.448$ Å) for the ensuing KI-CX study and a PBE-based optimization (giving $c = 8.560$ Å) for the KI-PBE(PBE) study.

Contrasting the KI-CX(CX) and KI-PBE(PBE) QP

results, we first focus on the valence bands along the symmetry path $G_v \rightarrow K_v \rightarrow M_v \rightarrow G_v$. At a general level, we find that use of KI-CX(CX) as our QP predictor lifts the near degeneracy found in KI-PBE(PBE) for the two top-most valence bands around the ‘K’, placing the VBM at the non-symmetric k -point T_v . We observe that this KI-CX(CX) VBM shift, $K_v \rightarrow T_v$, is in qualitative agreement with both KI-CX and the KI-PBE predictions obtained at the experimental value for the c lattice constant, Fig. 3, lower-right panel. That is, the change is primarily a consequence of structure and should be considered as an indirect effect of including vdW interactions. We add that this VBM shift is also found when dispersion-corrected HSE-D3 [100, 101, 132] is used to predict the band structure of the AA’ structure [75].

The shift to T_v of the QP VBM for the AA’ structure (bottom section of Table III) is caused by a general type of nonlocal-correlation (or beyond-pure-vdW) effect that we call incipient covalency [72, 138]. This VBM shift also arises for the AB structure, middle section of Table III and exists in bulk h-BN because the VBM orbitals have a pronounced p_z character [75], see Fig. 4. The fact that these occupied orbitals extend into the inter-layer regions means on the one hand that they enhance the vdW attraction [35] and on the other hand that such nonlocal-correlation effects drive a reduction of the interlayer separation (to close to the experimental c lattice constant of bulk h-BN) compared with descriptions by semilocal functionals [69, 123], e.g. PBE. The overall implication is that the DFT inclusion of the nonlocal-correlation term E_c^{nl} (sometimes equated as simply vdW forces) also – and in fact mainly – causes indirect QP signatures [124], for example, a small hybridization of slightly overlapping p_z orbitals originating from different layers.

In the upper hexagon of high-symmetry k -points in the BZ (corresponding to the A-H-L-A path), we note that use of KI-CX(CX) as our QP predictor generally causes only small shifts of KI-PBE-(PBE) predictions for the occupied-state energies; These shifts are upwards in some and downwards in other parts of this region of the BZ. However, in the paths of k points that connects the upper and lower parts of the irreducible BZ, we find that use of KI-CX(CX) causes QP-dispersion changes in the G_v - A_v and M_v - L_v variations.

The major differences between KI-CX(CX) and KI-PBE(PBE) predictions arise for the QP conduction bands, Fig. 6. For example, KI-CX(CX) predicts a ~ 3 eV larger dispersion in the BZ region near G (for the lowest-lying conduction bands). We find that KI-CX(CX) predicts a CBM at the M_c symmetry point, while the KI-PBE(PBE) predictor places it near G. The difference arises because KI-CX(CX) can be seen as raising the conduction-band QP values at the G_c point, making KI-CX(CX) consistent with GW on the CBM [76]. We can interpret these effects as again being mostly indirect vdW signatures. Nevertheless, even when we compared the KI-CX and KI-PBE at the same (experimental) structure, we did find some differences for the energy-

variation in QP conduction-band predictions.

Finally, we can interpret the accuracy of the KI-CX(CX) predictor in terms of vdW interactions producing a lowering of the $T_v \rightarrow M_c$ QP energy (6.47 eV). This is consistent with the observation that a closer (vdW-induced) proximity of the layers causes an overlap of the p_z orbitals, something that KI-PBE(PBE) entirely misses. Again, the absence of a consistent vdW and general nonlocal-correlation inclusion in KI-PBE(PBE) causes it to predict a $K_v \rightarrow G_c$ transition as the fundamental gap, at 7.32 eV.

D. Broader relevance of KI-CX usage

We observe that moving towards a full and consistent inclusion of vdW interactions in the descriptions of both QPs and GS structure and energies (the traditional role of DFT) is no easy task. Traditional MBPT methods, like GW, and wavefunction methods, like EOMCC, are today practical computational tools that can be used to characterize excited-state properties. However, these are costly compared to KI-DFT (that has the cost of DFPT) or gKS methods (that have the cost of hybrids). Also, a full capture of vdW-interaction effects requires self-consistent GW with vertex corrections (GWT) [139, 140]. Similarly, wave-function methods can predict charge-excited states with high accuracy, for example EOMCC for ionized states [6, 8, 9] or EOMCC for electron-attached states [7]. However, in such a framework, it is expected that the use of symmetry-adapted perturbation theory is necessary for incorporation of vdW effects [141, 142].

We consider KI-CX (which reduces to use of CX in KS-DFT when used for structure optimizations) as a faster alternative to GW and EOMCC studies when seeking to predict QPs and identify fingerprints of vdW interactions [3]. The CX functional is, as a conserving vdW-DF [35, 70, 71, 78], designed to capture the vdW interactions directly within the MBPT framework, as far as possible. Of course, it may not capture all nonlocal-correlation effects and that is why continued testing (e.g., via KI-CX predictions) is important.

We repeat our observation that KI-CX(CX) stands out by proceeding with the atomic-structure and QP characterizations in concert. As stated in the introduction, the CX (in KS-DFT) and KI-CX (in KI-DFT) use exactly the same MBPT input to define the nonempirical XC functional, per se. We think that a possible success of the CX design as a dual-use (KS-DFT and KI-DFT) functional, is helped by its inherent emphasis on current conservation and thus, the implied reflection of the plasmon nature. On the one hand, the plasmon-energy shifts by electro-dynamical coupling [35, 72] is a natural framework to count the integrated effects of nonlocal-correlation effects [71, 95]. On the other hand, a consistent modeling of virtual currents (as in plasmons) are essential when moving electrons (as in the excitations that QPs characterize).

Our interest in KI-CX goes well beyond the present fo-

cus on testing. By use of KI-CX we may be able to provide fast predictions of atomic and electronic (QP) structure in concert, for example, tracking fingerprints of vdW and, in general, noncovalent interactions in DNA systems while comparing with, e.g., optimally-tuned RSH vdW-DFs [23].

V. SUMMARY AND OUTLOOK

A comparative analysis of results reveals systematic trends across h-BN systems. The data is obtained by PBE and CX functions in KS-DFT functionals (denoted PBE, CX results) and with the corresponding use in KI-DFT (giving corresponding KI-PBE, KI-CX results). The performance is compared against *GW* results, where available. For both PBE and CX, we find that their use in KI-DFT consistently leads to better performance on QP descriptions that what their traditional (and originally intended) usage gives in KS-DFT.

For our present interest in systems with vdW and noncovalent binding, the KI-CX holds advantages over the traditional KI-PBE. We have considered both direct and indirect effects of the nonlocal-correlation effects on the QP. The former (latter) type of nonlocal-correlation effects are revealed when considering the QP band-structure predictions by KI-CX and KI-PBE at the same structure (when we consider the problem at the optimal atomic structure defined by KI-CX and KI-PBE). We find that KI-CX is significantly better than KI-PBE at QP predictions when we also use these functional to first predict the atomic structure.

Furthermore, we find that KI-CX delivers accuracy at QP predictions also when asserted on just the direct effects of including the vdW-type effects reflected in E_c^{nl} (i.e., when we compare KI-CX and KI-PBE at the same structure, fixed by experimental observations). For a summary, we focus on the quality at predicting the set of bulk-hBN QP gaps, i.e., energy differences between local QP-valence-band minima and local QP-conduction band maxima at various high-symmetry points of the Brillouin zone, e.g., G_c , K_c . While all of the investigated methods (use of CX or PBE in KS-DFT or as KI-CX and KI-PBE) exhibit transition-dependent errors (as asserted by comparison with GW), the KI-CX remains generally close to the GW values for the gaps. Overall, we find that the KI-CX results for the QP band structure validates the CX as a robust XC, performing also here at least as well as PBE.

We intend to use KI-CX to seek an acceleration of predictions of (ionizing) optical response of molecules, semiconductors and insulators. An advantage of using what we call consistent-KI-CX, or KI-CX(CX), lies in the fact that it is set up to predict QP in complex materials (cases when there is only a partial experimental characterization of atomic structure details). In those cases we need a robust, general-purpose vdW-DF, like CX, to first establish the details of atomic structure in KS-DFT. With

the KI-CX(CX) method, we argue that one can immediately extract predictions for QP properties (simply as KI-DFT states instead of KS-DFT states). This can, in principle, be done ahead of actual synthesis and ensuing structure predictions for general materials that are impacted by vdW forces.

ACKNOWLEDGMENTS

We thank Nicola Colonna and Edward Linscott for valuable discussions. The present work is supported by the Swedish Research Council (VR) through Grant No. 2022-03277, and by the Chalmers Area of Advance (AoA) Nano and Chalmers AoA Production. The computations were performed using computational and storage resources at Chalmers Centre for Computational Science and Engineering (C3SE), and with computer and storage allocations from the National Academic Infrastructure for Supercomputing in Sweden (NAISS), under contracts NAISS2023/3-22, NAISS2023/6-306, NAISS2024/3-16, and NAISS2024/6-432.

Appendix A: Linear response for nonlocal correlations

As mentioned in Section II.B, the DFPT response of the non-local potential $v^{\text{nl}}(\mathbf{r})$ is implemented in the KCW module of QE. The necessary linear-response steps are derived in Ref. 117 with respect to a general perturbation $\Delta^\lambda v^{\text{nl}}(\mathbf{r})$ and with the purpose (there) of computing vdW signatures on phonons and their interactions. Here, we summarize how this DFPT formulation for $\Delta^\lambda v^{\text{nl}}(\mathbf{r})$ appears when considered with respect to the removal or addition of a fractional electron, i.e., for KI-DFT use.

As a starting point, consider the definition of the non-local energy in Eq. (6), approximating the spatial integrals by sums over a uniform grid of points (at fixed positions ρ_i and \mathbf{r}_i) and the gradients by finite differences on the same grid. This allows the use of partial derivatives of the density variation on the grid to be used in place of formal functional derivatives [96]. Applying these finite differences and simplifying, we obtain:

$$E_c^{\text{nl}} = \sum_\alpha \sum_i u_{\alpha i}(\mathbf{r}_i) \Theta_{\alpha i}(\mathbf{r}_i), \quad (\text{A1})$$

where the first factor corresponds to the auxiliary function

$$u_{\alpha i} = \sum_\beta \sum_j \phi_{\alpha\beta}(\mathbf{r}_{ij}) \Theta_{\beta j}(\mathbf{r}_j).$$

Here, $\Theta_{\alpha i} = \rho_i P_\alpha[q(\rho_i, |\nabla\rho_i|)]$, the values q_α are chosen to ensure accurate interpolation of the function ϕ , and P_α is the function resulting from the interpolation.

From Eq. (A1), one can obtain the non-local potential ($\partial E_c^{\text{nl}}/\partial\rho$) in a more compact notation:

$$\begin{aligned} v_i^{\text{nl}} &= \sum_\alpha \left[\left(u_{\alpha i} \frac{\partial \Theta_{\alpha i}}{\partial \rho_i} \right) + \sum_j u_{\alpha j} \left(\frac{\partial \Theta_{\alpha j}}{\partial |\nabla \rho_j|} \frac{\partial |\nabla \rho_j|}{\partial \rho_i} \right) \right] \\ &\equiv b_i + \sum_j h_j, \end{aligned} \quad (\text{A2})$$

where b_i corresponds a term defined exclusively by differentiating direct by density (at the specific grid site i). The second term, defined by a set of h_j contributions, reflects instead derivations with respect to the density gradients. The evaluation of a gradient in QE makes use of specific stencil so that the gradient at site i can be expressed in terms of the density values at neighboring grid sites j [96].

To obtain the non-local response kernel for E_c^{nl} , Eq. (10), it is necessary to apply DFPT to Eq. (6). To do this, consider an infinitesimal fraction of an electron $\delta\mathbf{0}n$ added or removed to the n th MLWF at $\mathbf{0}$. This generates a perturbation in the effective KS potential $\Delta^{\delta\mathbf{0}n} v_{\text{KS}}$, leading, in turn to a new variation of the density, with relative changes denoted $\Delta^{\delta\mathbf{0}n} \rho(\mathbf{r})$. The first-order change in this non-local potential is:

$$\Delta^{\delta\mathbf{0}n} v_i^{\text{nl}} = \sum_j \frac{\partial v_i^{\text{nl}}}{\partial \rho_j} \Delta^{\delta\mathbf{0}n} \rho_j. \quad (\text{A3})$$

Expressing also the v_i^{nl} for in Ref. (A3) reveals the second derivatives present in Eq. (10). To get a numerical evaluation, we adapt the grid-specific implementation [81, 96, 117] of the formal determination

$$\sum_{ij} \frac{\partial^2 E_c^{\text{nl}}[\rho_i]}{\partial \rho_i \partial \rho_j} \Delta^{\delta\mathbf{0}n} \rho_j \approx \iint d\mathbf{r} d\mathbf{r}' \frac{\delta^2 E_c^{\text{nl}}}{\delta \rho(\mathbf{r}) \delta \rho(\mathbf{r}')} \Delta^{\delta\mathbf{0}n} \rho(\mathbf{r}'). \quad (\text{A4})$$

Finally, to get the DFPT, we can simply linearize the two components of Eq. (A3):

$$\Delta^{\delta\mathbf{0}n} v^{\text{nl}} = \sum_i \left(\frac{\partial b_j}{\partial \rho_i} + \sum_k \frac{\partial b_k}{\partial \rho_i} \right) \Delta^{\delta\mathbf{0}n} \rho_i. \quad (\text{A5})$$

The details of these two components are explicitly derived, for the stencil used in QE, in Ref. 117.

In summary, KI-DFT in QE is in fact already set up to move to a KI-CX(CX) form and general-purpose starting point for QP characterizations, as here illustrated.

Appendix B: Precision in KI-CX

For KS-DFT studies using norm-conserving pseudopotentials, past experience suggest that a choice $E_{\text{cut}}^{\text{wf}} = 200$ Ry for wavefunction kinetic-energy cut off is sufficient to converge predictions of total-energy differences and structure [23, 74].

c [Å]	N_k^{\parallel}	$E_{\text{cut}}^{\text{wf}}$ [Ry]	$G_v \rightarrow G_c$	$M_v \rightarrow M_c$	$K_v \rightarrow G_c$	$K_v \rightarrow K_c$	$M_v \rightarrow G_c$	$K_v \rightarrow M_c$
20	7	100	7.62	8.98	5.90	7.94	6.79	8.08
20	7	200	8.14	9.90	6.42	8.61	7.31	9.00
20	7	300	8.18	9.86	6.46	8.62	7.36	8.96
<i>20</i>	<i>7</i>	<i>400</i>	<i>8.21</i>	<i>9.92</i>	<i>6.48</i>	<i>8.69</i>	<i>7.38</i>	<i>9.02</i>
30	7	100	8.36	10.01	6.63	8.81	7.53	9.11
30	7	200	8.28	9.95	6.55	8.65	7.45	9.05
30	7	300	8.28	10.17	6.56	8.89	7.45	9.27
30	7	400	8.20	9.99	6.47	8.72	7.37	9.09
20	7	200	8.14	9.90	6.42	8.61	7.31	9.00
20	9	200	7.70	8.90	5.94	8.01	6.85	7.99
20	11	200	8.08	9.59	6.32	8.40	7.23	8.67
<i>20</i>	<i>7</i>	<i>400</i>	<i>8.21</i>	<i>9.92</i>	<i>6.48</i>	<i>8.69</i>	<i>7.38</i>	<i>9.02</i>
20	9	400	8.34	9.58	6.58	8.75	7.49	8.66
20	11	400	7.69	9.15	5.93	7.93	6.84	8.24

TABLE IV. Search for precision (numerical stability with respect to choice of modeling parameters) in KI-CX predictions of BN1 QP-gap energies (in eV) as defined by transitions between indicated valence- and conduction-band symmetry points. Italicized table entries identify the set of model parameters that we use, in the main text, to report and discuss the QP behavior for the strictly two-dimensional BN1 system.

$E_{\text{cut}}^{\text{wf}}$ [Ry]	$G_v \rightarrow G_c$	$M_v \rightarrow M_c$	$K_v \rightarrow G_c$	$K_v \rightarrow K_c$	$M_v \rightarrow G_c$	$K_v \rightarrow M_c$	Fundamental Gap
150 ^a	9.14	7.06	7.50	7.46	7.85	6.71	6.58 ^b
200 ^a	9.14	7.06	7.50	7.46	7.85	6.71	6.58 ^b
250 ^a	9.14	7.06	7.50	7.46	7.85	6.71	6.58 ^b
300 ^a	9.14	7.06	7.50	7.46	7.85	6.71	6.59 ^b
350 ^a	8.84	7.41	7.20	7.46	7.55	7.07	6.93 ^b
GW^c	8.40	6.50	6.90	6.90	7.30	-	5.95 ^b
Exper. ^d	-	-	-	-	-	-	6.08

^a KI-CX with $7 \times 7 \times 3$ k -point sampling.
^b Corresponds to $T_v \rightarrow M_c$.
^c Ref. 76.
^d Ref. 131.

TABLE V. **FOR here but not in archive and submitted versions unless surprise with double checks.** QP gap predictions (in eV) by KI-CX for h-BN bulk structure AA' as a function of the choice of the choice of the wavefunction-energy cut off $E_{\text{cut}}^{\text{wf}}$. The highlighted parameter choice identify the pick we made for discussing the nature and and energy variation of QPs in bulk-h-BN characterization in the main text.

We find that the same choice also consistently leads to robust predictions for the valence-type QP energies. This is expected and can be understood from the following observations. First, the KS-DFT studies can only converge the total energy and the density variation when the spatial variation in the occupied KS-DFT orbitals are all themselves converged. Second, we find vanishing differences, besides an overall energy shifts, between the valence band structure as described in, for example, CX and KI-CX. Our experience is that the process of making the MLWF representations, and hence the completion of the KI-CX functional specification, is inherently robust for descriptions of the set of occupied QPs states.

For descriptions of conduction-band QP states we see a need to secure numerical stability with regards to changes in the choice of implicit modeling parameters; This observation has practical implications for our KI-CX study of the single-sheet BN1 system. The description of unoccupied QPs is generally a challenge for KS-DFT, for example, documented for electron attachment in nitrogen-base

systems [23, 60]. This problem emerges, in part, because the spatial variation of unoccupied KS-orbitals does not naturally enter in the iterative optimization of the actual ground-state electron density $\rho(\mathbf{r})$. In contrast, with a hybrid like AHBR-mRSH and with the KI-DFT framework, we can overcome also this KS-DFT problem to accurately describe the empty QPs [23, 60] because we make the iterative computational scheme dependent on the nature of these empty orbitals. However, the requirements on the $E_{\text{cut}}^{\text{wf}}$ choice for stability in the description of conduction-band states might well be higher. Also, given our screening handling [125], we must validate that the chosen height c of the modeling cell for the strictly two-dimensional BN1 system is sufficient to electrically decouple the sheets.

Table IV presents an overview of the numerical work we completed to assert the level of precision we presently have for a KI-DFT description of (empty-state) QP energies in BN1. We see that the step of crafting of the MLWF representation for KI-DFT use can sometimes

cause abrupt changes in predictions of conduction-band QP energies. A complication is that the $E_{\text{cut}}^{\text{wf}}$ variation also depends on the choice of c . Our criteria for reporting BN1 QP predictions is that we reach a fair numerical stability with regards to changes in both of these modeling parameters. Tables II and IV report our finding that we have a fair level of cross-checked stability for the conduction-band QPs of BN1 when using $c = 20 \text{ \AA}$ and $E_{\text{cut}}^{\text{wf}} = 400 \text{ Ry}$, as also stated in the main text.

NOTE: The choice of N_{\parallel} in a set of possible $N_k^{\parallel} \times N_k^{\parallel} \times 1$ samplings of k points for in BN1 predictions has also been tested. If the choice of $N_k^{\parallel} = 7$ is sufficient to reflect a plateau of BN1 predictions also in the modeling aspect,

as is suggested in Table IV, then we shall merely state that as a comment here in the appendix text.

NOTE: Table V summarizes a study of numerical stability for the AA' bulk system. This table will not be in arXiv or submitted version BUT it is convenient to have here for overview in house.

We also performed a study of numerical stability for the bulk AA' system in KI-CX. We found no variation in predictions for QP gap results as we increased $E_{\text{cut}}^{\text{wf}}$ from 150 Ry to 300 Ry. Accordingly we chose to complete all KI-DFT characterizations for bulk h-BN at the value $E_{\text{cut}}^{\text{wf}} = 200 \text{ Ry}$ that is adequate for total-energy and structure characterizations in KS-DFT.

-
- [1] W. G. Aulbur, L. Jönsson, and J. W. Wilkins, Quasiparticle Calculations in Solids, in *Solid State Physics*, Vol. 54, edited by F. Seitz, D. Turnbull, and H. Ehrenreich (Academic Press, New York, 2000) p. 1.
- [2] S. Ornes, Quasiparticle, Proc. Natl.Acad.Sci. **111**, 15601 (2014).
- [3] T. Rangel, K. Berland, S. Sharifzadeh, F. Brown-Altvater, K. Lee, P. Hyldgaard, L. Kronik, and J. B. Neaton, Structural and excited-state properties of oligoacene crystals from first principles, Phys. Rev. B **93**, 115206 (2016).
- [4] L. Hedin, New method for calculating the one-particle green's function with application to the electron-gas problem, Phys. Rev. **139**, A796 (1965).
- [5] L. Reining, The GW approximation: content, successes and limitations, WIREs. Comput. Mol. Sci. **8**, e1344 (2018).
- [6] J. F. Stanton and J. Gauss, Analytic energy derivatives for ionized states described by the equation-of-motion coupled cluster method, J. Chem. Phys. **101**, 8938 (1994).
- [7] M. Nooijen and R. J. Bartlett, Equation of motion coupled cluster method for electron attachment, J. Chem. Phys. **102**, 3629 (1995).
- [8] R. J. Bartlett, J. E. Del Bene, S. Perera, and R. Mattie, Ammonia: the prototypical lone pair molecule, J. Mol. Struct. THEOCHEM **400**, 157 (1997), ab Initio Benchmark Studies.
- [9] R. Quintero-Monsebaiz and P.-F. Loos, Equation generator for equation-of-motion coupled cluster assisted by computer algebra system, AIP Adv. **13**, 085035 (2023).
- [10] P. Hohenberg and W. Kohn, Inhomogeneous electron gas, Phys. Rev. **136**, B864 (1964).
- [11] W. Kohn and L. J. Sham, Self-consistent equations including exchange and correlation effects, Phys. Rev. **140**, A1133 (1965).
- [12] O. Gunnarsson and R. O. Jones, Density Functional Calculations for Atoms, Molecules and Clusters, Phys. Scripta **21**, 394 (1980).
- [13] J. M. Seminario, An introduction to density functional theory in chemistry, in *Modern Density Functional Theory: A Tool for Chemistry*, Theoretical and Computational Chemistry, Vol. 2, edited by J. Seminario and P. Politzer (Elsevier, 1995) pp. 1–27.
- [14] K. Burke and L. O. Wagner, DFT in a nutshell, Int. J. Quantum Chem. **113**, 96 (2013).
- [15] A. Seidl, A. Görling, P. Vogl, J. A. Majewski, and M. Levy, Generalized Kohn-Sham schemes and the band-gap problem, Phys. Rev. B **53**, 3764 (1996).
- [16] L. Kronik, T. Stein, S. Refaely-Abramson, and R. Baer, Excitation gaps of finite-sized systems from optimally tuned range-separated hybrid functionals, J. Chem. Theory Comput. **8**, 1515 (2012).
- [17] J. P. Perdew, M. Ernzerhof, and K. Burke, Rationale for mixing exact exchange with density functional approximations, J. Chem. Phys. **105**, 9982 (1996).
- [18] S. Refaely-Abramson, S. Sharifzadeh, N. Govind, J. Autschbach, J. B. Neaton, R. Baer, and L. Kronik, Quasiparticle spectra from a nonempirical optimally tuned range-separated hybrid density functional, Phys. Rev. Lett. **109**, 226405 (2012).
- [19] W. Chen, G. Miceli, G.-M. Rignanese, and A. Pasquarello, Nonempirical dielectric-dependent hybrid functional with range separation for semiconductors and insulators, Phys. Rev. Mater. **2**, 073803 (2018).
- [20] J. H. Skone, M. Govoni, and G. Galli, Nonempirical range-separated hybrid functionals for solids and molecules, Phys. Rev. B **93**, 235106 (2016).
- [21] D. Wing, G. Ohad, J. B. Haber, M. R. Filip, S. E. Gant, J. B. Neaton, and L. Kronik, Band gaps of crystalline solids from Wannier-localization-based optimal tuning of a screened range-separated hybrid functional, PNAS **118**, e2104556118 (2021).
- [22] V. Shukla, Y. Jiao, C. M. Frostenson, and P. Hyldgaard, vdW-DF-ahcx: a range-separated van der Waals density functional hybrid, J. Phys.: Condens. Matter. **34**, 025902 (2021).
- [23] E. Schröder, R. Quintero-Monsebaiz, Y. Jiao, and P. Hyldgaard, Optimally tuned range-separated hybrid van der waals density functional for molecular binding and quasiparticle characterizations, J. Phys.: Condens. Matter. **37**, 211501 (2025).
- [24] I. Dabo, A. Ferretti, N. Poilvert, Y. Li, N. Marzari, and M. Cococcioni, Koopmans' condition for density-functional theory, Phys. Rev. B **82**, 115121 (2010).
- [25] A. Ferretti, I. Dabo, M. Cococcioni, and N. Marzari, Bridging density-functional and many-body perturbation theory: Orbital-density dependence in electronic-structure functionals, Phys. Rev. B **89**, 195134 (2014).

- [26] G. Borghi, A. Ferretti, N. L. Nguyen, I. Dabo, and N. Marzari, Koopmans-compliant functionals and their performance against reference molecular data, *Phys. Rev. B*, 075135 (2018).
- [27] R. De Gennaro, N. Colonna, E. Linscott, and N. Marzari, Bloch's theorem in orbital-density-dependent functionals: Band structures from Koopmans spectral functionals, *Phys. Rev. B* **106**, 035106 (2022).
- [28] N. Colonna, R. De Gennaro, E. Linscott, and N. Marzari, Koopmans spectral functionals in periodic boundary conditions, *J. Chem. Theory Comput.* **18**, 5435 (2022).
- [29] E. B. Linscott, N. Colonna, R. De Gennaro, N. L. Nguyen, G. Borghi, A. Ferretti, I. Dabo, and N. Marzari, koopmans: An Open Source Package for Accurately and Efficiently Predicting Spectral Properties with Koopmans Functionals, *J. Chem. Theory Comput.* **19**, 7097 (2023).
- [30] E. B. Linscott, N. Colonna, R. De Gennaro, N. L. Nguyen, G. Borghi, A. Ferretti, I. Dabo, and N. Marzari, Koopmans Functionals Documentation, <https://koopmans-functionals.org/en/latest/> (2025), accessed: 2025-07-21.
- [31] L. Hedin and S. Lundqvist, Effects of electron-electron and electron-phonon interactions on the one-electron states of solids, in *Solid State Physics*, Vol. 23, edited by F. Seitz, D. Turnbull, and H. Ehrenreich (Academic Press, New York, 1969) p. 1.
- [32] L. Hedin and B. I. Lundqvist, Explicit local exchange-correlation potentials, *J. Phys. C* **4**, 2064 (1971).
- [33] L. J. Sham and M. Schlüter, Density-Functional Theory of the Energy Gap, *Phys. Rev. Lett.* **51**, 1888 (1983).
- [34] M. E. Casida, Generalization of the optimized-effective-potential model to include electron correlation: A variational derivation of the Sham-Schlüter equation for the exact exchange-correlation potential, *Phys. Rev. A* **51**, 2005 (1999).
- [35] P. Hyldgaard, Y. Jiao, and V. Shukla, Screening nature of the van der Waals density functional method: a review and analysis of the many-body physics foundation, *J. Phys.: Condens. Matter.* **32**, 393001 (2020).
- [36] S. Ma and K. Brueckner, Correlation energy of an electron gas with a slowly varying high density, *Phys. Rev.* **165**, 18 (1968).
- [37] D. C. Langreth, Singularities in the x-ray spectra of metals, *Phys. Rev. B* **1**, 471 (1970).
- [38] D. Langreth and J. Perdew, The exchange-correlation energy of a metallic surface, *Solid State Commun.* **17**, 1425 (1975).
- [39] O. Gunnarsson and B. I. Lundqvist, Exchange and correlation in atoms, molecules, and solids by the spin-density-functional formalism, *Phys. Rev. B* **13**, 4274 (1976).
- [40] D. C. Langreth and J. P. Perdew, Exchange-correlation energy of a metallic surface: Wave-vector analysis, *Phys. Rev. B* **15**, 2884 (1977).
- [41] D. C. Langreth and J. P. Perdew, Theory of nonuniform electronic systems. I. Analysis of the gradient approximation and a generalization that works, *Phys. Rev. B* **21**, 5469 (1980).
- [42] D. C. Langreth and M. J. Mehl, Easily implementable nonlocal exchange-correlation energy functional, *Phys. Rev. Lett.* **47**, 446 (1981).
- [43] D. C. Langreth and S. H. Vosko, Exact electron-gas response functions at high density, *Phys. Rev. Lett.* **59**, 497 (1987).
- [44] D. C. Langreth and S. Vosko, Response functions and nonlocal approximations, in *Density Functional Theory of Many-Fermion Systems*, Advances in Quantum Chemistry, Vol. 21, edited by P.-O. Löwdin (Academic Press, 1990) pp. 175–199.
- [45] J. P. Perdew, K. Burke, and M. Ernzerhof, Generalized Gradient Approximation Made Simple, *Phys. Rev. Lett.* **77**, 3865 (1996).
- [46] T. Thonhauser, V. R. Cooper, S. Li, A. Puzder, P. Hyldgaard, and D. C. Langreth, van der Waals density functional: Self-consistent potential and the nature of the van der Waals bond, *Phys. Rev. B* **76**, 125112 (2007).
- [47] D. P. Chong, O. V. Gritsenko, and E. J. Baerends, Interpretation of the Kohn–Sham orbital energies as approximate vertical ionization potentials, *J. Chem. Phys.* **116**, 1760 (2002).
- [48] M. Cococcioni and S. de Gironcoli, Linear response approach to the calculation of the effective interaction parameters in the LDA + U method, *Phys. Rev. B* **71**, 035105 (2005).
- [49] N. L. Nguyen, N. Colonna, A. Ferretti, and N. Marzari, Koopmans-compliant spectral functionals for extended systems, *Phys. Rev. X* **8**, 021051 (2018).
- [50] F. Brown-Altwater, T. Rangel, and J. B. Neaton, Ab initio phonon dispersion in crystalline naphthalene using van der Waals density functionals, *Phys. Rev. B* **93**, 195206 (2016).
- [51] E. J. Granhed, G. Wahnström, and P. Hyldgaard, BaZrO₃ stability under pressure: the role of non-local exchange and correlation, *Phys. Rev. B* **101**, 224105 (2020).
- [52] A. Perrichon, E. J. Granhed, G. Romanelli, A. Piovano, A. Lindman, P. Hyldgaard, G. Wahnström, and M. Karlsson, Unraveling the ground-state structure of BaZrO₃ by neutron scattering experiments and first-principle calculations, *Chem. Mater.* **32**, 2824 (2020).
- [53] P. Y. Yu and M. Cardona, Electrical transport, in *Fundamentals of Semiconductors: Physics and Materials Properties* (Springer Berlin Heidelberg, Berlin, Heidelberg, 2010) pp. 203–241.
- [54] S. N. Magonov, Surface Characterization of Materials at Ambient Conditions by Scanning Tunneling Microscopy (STM) and Atomic Force Microscopy (AFM), *Appl. Spectrosc. Rev.* **28**, 1 (1993).
- [55] H. Zhang, T. Pincelli, C. Jozwiak, T. Kondo, R. Ernstorfer, T. Sato, and S. Zhou, Angle-resolved photoemission spectroscopy, *NRMP* **2**, 54 (2022).
- [56] W. Grünert and K. Klementiev, X-ray absorption spectroscopy principles and practical use in materials analysis, *Phys. Sci. Rev.* **5**, 20170181 (2020).
- [57] N. V. Smith, Inverse photoemission, *Rep. Prog. Phys.* **51**, 1227 (1988).
- [58] I. Dabo, A. Ferretti, C.-H. Park, N. Poilvert, Y. Li, M. Cococcioni, and N. Marzari, Donor and acceptor levels of organic photovoltaic compounds from first principles, *Phys. Chem. Chem. Phys.* **15**, 685 (2013).
- [59] N. L. Nguyen, G. Borghi, A. Ferretti, I. Dabo, and N. Marzari, First-Principles Photoemission Spectroscopy and Orbital Tomography in Molecules from Koopmans-Compliant Functionals, *Phys. Rev. Lett.*

- 114**, 166405 (2015).
- [60] N. L. Nguyen, G. Borghi, A. Ferretti, and N. Marzari, First-Principles Photoemission Spectroscopy of DNA and RNA Nucleobases from Koopmans-Compliant Functionals, *J. Chem. Theory Comput.* **12**, 3948 (2016).
- [61] N. Colonna, N. L. Nguyen, A. Ferretti, and N. Marzari, Screening in Orbital-Density-Density Functionals, *J. Chem. Theory Comput.* **14**, 2549 (2018).
- [62] N. Colonna, N. L. Nguyen, A. Ferretti, and N. Marzari, Koopmans-Compliant Functionals and Potentials and their applications to the GW100 Test Set, *J. Chem. Theory Comput.* **15**, 1905 (2019).
- [63] J. D. Elliott, N. Colonna, M. Marsili, N. Marzari, and P. Umara, Koopmans Meets Bethe–Salpeter: Excitonic Optical Spectra without GW, *J. Chem. Theory Comput.* **15**, 3710 (2019).
- [64] J. M. de Almeida, N. L. Nguyen, N. Colonna, W. Chen, C. R. Miranda, A. Pasquarello, and N. Marzari, Electronic Structure of Water from Koopmans-Compliant Functionals, *J. Chem. Theory Comput.* **17**, 3923 (2019).
- [65] A. Marrazzo and N. Colonna, Spin-dependent interactions in orbital-density-dependent functionals: Non-collinear Koopmans spectral functionals, *Phys. Rev. Research* **6**, 033085 (2024).
- [66] J. P. Perdew and Y. Wang, Pair-distribution function and its coupling-constant average for the spin-polarized electron gas, *Phys. Rev. B* **46**, 12947 (1992).
- [67] J. P. Perdew, R. G. Parr, M. Levy, and J. L. Balduz, Density-Functional Theory for Fractional Particle Number: Derivative Discontinuities of the Energy, *Phys. Rev. Lett.* **49**, 1691 (1982).
- [68] Y. Schubert, N. Marzari, and E. Linscott, Testing Koopmans spectral functionals on the analytically solvable Hooke’s atom, *J. Chem. Phys.* **158**, 144113 (2023).
- [69] H. Rydberg, M. Dion, N. Jacobson, E. Schröder, P. Hyldgaard, S. I. Simak, D. C. Langreth, and B. I. Lundqvist, Van der Waals Density Functional for Layered Structures, *Phys. Rev. Lett.* **91**, 126402 (2003).
- [70] M. Dion, H. Rydberg, E. Schröder, D. C. Langreth, and B. I. Lundqvist, van der Waals Density Functional for General Geometries, *Phys. Rev. Lett.* **92**, 246401 (2004).
- [71] P. Hyldgaard, K. Berland, and E. Schröder, Interpretation of van der Waals density functionals, *Phys. Rev. B* **90**, 075148 (2014).
- [72] K. Berland, V. R. Cooper, K. Lee, E. Schröder, T. Thonhauser, P. Hyldgaard, and B. I. Lundqvist, van der Waals forces in density functional theory: a review of the vdW-DF method, *Rep. Prog. Phys.* **78**, 066501 (2015).
- [73] T. Thonhauser, S. Zuluaga, C. A. Arter, K. Berland, E. Schröder, and P. Hyldgaard, Spin Signature of Nonlocal Correlation Binding in Metal-Organic Frameworks, *Phys. Rev. Lett.* **115**, 136402 (2015).
- [74] V. Shukla, Y. Jiao, J.-H. Lee, E. Schröder, J. B. Neaton, and P. Hyldgaard, Accurate Nonempirical Range-Separated Hybrid van der Waals Density Functional for Complex Molecular Problems, Solids, and Surfaces, *Phys. Rev. X* **12**, 041003 (2022).
- [75] D. Wickramaratne, L. Weston, and C. G. Van de Walle, Monolayer to Bulk Properties of Hexagonal Boron Nitride, *J. Phys. Chem. C* **122**, 25524 (2018).
- [76] R. J. Hunt, B. Monserrat, V. Zólyomi, and N. D. Drummond, Diffusion quantum Monte Carlo and *GW* study of the electronic properties of monolayer and bulk hexagonal boron nitride, *Phys. Rev. B* **101**, 205115 (2020).
- [77] H. Rydberg, B. I. Lundqvist, D. C. Langreth, and M. Dion, Tractable nonlocal correlation density functionals for flat surfaces and slabs, *Phys. Rev. B* **62**, 6997 (2000).
- [78] K. Berland and P. Hyldgaard, Exchange functional that tests the robustness of the plasmon description of the van der Waals density functional, *Phys. Rev. B* **89**, 035412 (2014).
- [79] K. Berland, C. A. Arter, V. R. Cooper, K. Lee, B. I. Lundqvist, E. Schröder, T. Thonhauser, and P. Hyldgaard, van der Waals density functionals built upon the electron-gas tradition: Facing the challenge of competing interactions, *J. Chem. Phys.* **140**, 18A539 (2014).
- [80] P. Giannozzi, S. Baroni, N. Bonini, M. Calandra, R. Car, C. Cavazzoni, D. Ceresoli, G. L. Chiarotti, M. Cococcioni, I. Dabo, A. D. Corso, S. de Gironcoli, S. Fabris, G. Fratesi, R. Gebauer, U. Gerstmann, C. Gougoussis, A. Kokalj, M. Lazzeri, L. Martin-Samos, N. Marzari, F. Mauri, R. Mazzarello, S. Paolini, A. Pasquarello, L. Paulatto, C. Sbraccia, S. Scandolo, G. Sciauzero, A. P. Seitsonen, A. Smogunov, P. Umari, and R. M. Wentzcovitch, QUANTUM ESPRESSO: a modular and open-source software project for quantum simulations of materials, *J. Phys.: Condens. Matter.* **21**, 395502 (2009).
- [81] P. Giannozzi, O. Andreussi, T. Brumme, O. Bunau, M. B. Nardelli, M. Calandra, R. Car, C. Cavazzoni, D. Ceresoli, M. Cococcioni, N. Colonna, I. Carnimeo, A. D. Corso, S. de Gironcoli, P. Delugas, R. A. DiStasio, A. Ferretti, A. Floris, G. Fratesi, G. Fugallo, R. Gebauer, U. Gerstmann, F. Giustino, T. Gorni, J. Jia, M. Kawamura, H.-Y. Ko, A. Kokalj, E. Küçükbenli, M. Lazzeri, M. Marsili, N. Marzari, F. Mauri, N. L. Nguyen, H.-V. Nguyen, A. O. de-la Roza, L. Paulatto, S. Poncé, D. Rocca, R. Sabatini, B. Santra, M. Schlipf, A. P. Seitsonen, A. Smogunov, I. Timrov, T. Thonhauser, P. Umari, N. Vast, X. Wu, and S. Baroni, Advanced capabilities for materials modelling with Quantum ESPRESSO, *J. Phys.: Condens. Matter.* **29**, 465901 (2017).
- [82] J. D. Caldwell, I. Aharonovich, G. Cassabois, J. H. Edgar, B. Gil, and D. N. Basov, Photonics with hexagonal boron nitride, *Nat. Rev. Mater.* **4**, 552 (2019).
- [83] S. Roy, X. Zhang, A. B. Puthirath, A. Meiyazhagan, S. Bhattacharyya, M. M. Rahman, G. Babu, S. Susarla, S. K. Saju, M. K. Tran, L. M. Sassi, M. A. S. R. Saadi, J. Lai, O. Sahin, S. M. Sajadi, B. Dharmarajan, D. Salpekar, N. Chakingal, A. Baburaj, X. Shuai, A. Adumbukulath, K. A. Miller, J. M. Gayle, A. Ajnsztajn, T. Prasankumar, V. V. J. Harikrishnan, V. Ojha, H. Kannan, A. Z. Khater, Z. Zhu, S. A. Iyengar, P. A. d. S. Autreto, E. F. Oliveira, G. Gao, A. G. Birdwell, M. R. Neupane, T. G. Ivanov, J. Taha-Tijerina, R. M. Yadav, S. Arepalli, R. Vajtai, and P. M. Ajayan, Structure, Properties and Applications of Two-Dimensional Hexagonal Boron Nitride, *Adv. Mater.* **33**, 2101589 (2021).
- [84] L. Lindsay and D. A. Broido, Enhanced thermal conductivity and isotope effect in single-layer hexagonal boron

- nitride, *Phys. Rev. B* **84**, 155421 (2011).
- [85] C. Li, Y. Bando, C. Zhi, Y. Huang, and D. Golberg, Thickness-dependent bending modulus of hexagonal boron nitride nanosheets, *Nat. Nanotechnol.* **20**, 385707 (2009).
- [86] Q. Weng, X. Wang, X. Wang, Y. Bando, and D. Golberg, Functionalized hexagonal boron nitride nanomaterials: emerging properties and applications, *Chem. Soc. Rev.* **45**, 3989 (2016).
- [87] A. Zunger, A. Katzir, and A. Halperin, Optical properties of hexagonal boron nitride, *Phys. Rev. B* **13**, 5560 (1976).
- [88] C. Yu, J. Zhang, W. Tian, X. Fan, and Y. Yao, Polymer composites based on hexagonal boron nitride and their application in thermally conductive composites, *RSC Adv.* **8**, 21948 (2018).
- [89] K. Zhang, Y. Feng, F. Wang, Z. Yang, and J. Wang, Two dimensional hexagonal boron nitride (2D-hBN): synthesis, properties and applications, *J. Mater. Chem. C* **5**, 11992 (2017).
- [90] M. Li, G. Huang, X. Chen, J. Yin, P. Zhang, Y. Yao, J. Shen, Y. Wu, and J. Huang, Perspectives on environmental applications of hexagonal boron nitride nanomaterials, *Nano Today* **44**, 101486 (2022).
- [91] O. Gunnarsson and B. I. Lundqvist, Erratum: Exchange and correlation in atoms, molecules, and solids by the spin-density-functional formalism, *Phys. Rev. B* **15**, 6006 (1977).
- [92] J. P. Perdew and Y. Wang, Accurate and simple density functional for the electronic exchange energy: Generalized gradient approximation, *Phys. Rev. B* **33**, 8800 (1986).
- [93] K. Lee, È. D. Murray, L. Kong, B. I. Lundqvist, and D. C. Langreth, Higher-accuracy van der Waals density functional, *Phys. Rev. B* **82**, 081101 (2010).
- [94] D. Chakraborty, K. Berland, and T. Thonhauser, Next-Generation Nonlocal van der Waals Density Functional, *J. Chem. Theory Comput.* **16**, 5893 (2020).
- [95] G. D. Mahan, van der Waals forces in solids, *J. Chem. Phys.* **43**, 1569 (1965).
- [96] G. Román-Pérez and J. M. Soler, Efficient Implementation of a van der Waals Density Functional: Application to Double-Wall Carbon Nanotubes, *Phys. Rev. Lett.* **103**, 096102 (2009).
- [97] M. Levy, J. P. Perdew, and V. Sahni, Exact differential equation for the density and ionization energy of a many-particle system, *Phys. Rev. A* **30**, 2745 (1984).
- [98] K. Berland, Y. Jiao, J.-H. Lee, T. Rangel, J. B. Neaton, and P. Hyldgaard, Assessment of two hybrid van der Waals density functionals for covalent and noncovalent binding of molecules, *J. Chem. Phys.* **146**, 234106 (2017).
- [99] Y. Jiao, E. Schröder, and P. Hyldgaard, Extent of Fock-exchange mixing for a hybrid van der Waals density functional?, *J. Chem. Phys.* **148**, 194115 (2018).
- [100] J. Heyd, G. E. Scuseria, and M. Ernzerhof, Hybrid functionals based on a screened coulomb potential, *J. Chem. Phys.* **118**, 8207 (2003).
- [101] J. Heyd, G. E. Scuseria, and M. Ernzerhof, Erratum: "hybrid functionals based on a screened coulomb potential" [*J. Chem. Phys.* 118, 8207 (2003)], *J. Chem. Phys.* **124**, 219906 (2006).
- [102] C. M. Frostenson, E. J. Granhed, V. Shukla, P. A. T. Olsson, E. Schröder, and P. Hyldgaard, Hard and soft materials: putting consistent van der Waals density functionals to work, *Electron. Struct.* **4**, 014001 (2022).
- [103] C. Frostenson, Y. Feng, P. Hyldgaard, and H. Grönbeck, Range-separated hybrid van der Waals density functionals to describe Cu_2O_2 -complexes, *Chem. Phys. Lett.* **856**, 141589 (2024).
- [104] I. Hamada, van der Waals density functional made accurate, *Phys. Rev. B* **89**, 121103 (2014).
- [105] S. Rafaely-Abramson, S. Sharifzadeh, M. Jain, R. Baer, J. B. Neaton, and L. Kronik, Gap renormalization of molecular crystals from density functional theory, *Phys. Rev. B* **88**, 081204(R) (2013).
- [106] L. Lin, Adaptively compressed exchange operator, *J. Chem. Theory Comput.* **12**, 2242 (2016).
- [107] I. Carnimeo, S. Baroni, and P. Giannozzi, Fast hybrid density-functional computations using plane-wave basis sets, *Electron. Struct.* **1**, 015009 (2019).
- [108] Z.-F. Liu, D. A. Egger, S. Rafaely-Abramson, and L. K. J. B. Neaton, Energy level alignment at molecule-metal interfaces from an optimally tuned range-separated hybrid functional, *J. Chem. Phys.* **146**, 092326 (2017).
- [109] A. I. Liechtenstein, V. I. Anisimov, and J. Zaanen, Density-functional theory and strong interactions: Orbital ordering in mott-hubbard insulators, *Phys. Rev. B* **52**, R5467 (1995).
- [110] S. L. Dudarev, G. A. Botton, S. Y. Savrasov, C. J. Humphreys, and A. P. Sutton, Electron-energy-loss spectra and the structural stability of nickel oxide: An *l*sd_a+*u* study, *Phys. Rev. B* **57**, 1505 (1998).
- [111] H. Peng and J. P. Perdew, Synergy of van der Waals and self-interaction corrections in transition metal monoxides, *Phys. Rev. B* **96**, 100101(R) (2017).
- [112] K. Burke, M. Ernzerhof, and J. P. Perdew, The adiabatic connection method: a non-empirical hybrid, *Chem. Phys. Lett.* **265**, 115 (1997).
- [113] Y. Jiao, E. Schröder, and P. Hyldgaard, Signature of van der Waals binding: A coupling-constant scaling analysis, *Phys. Rev. B* **97**, 085115 (2018).
- [114] S. Racioppi, P. Lolur, P. Hyldgaard, and M. Rahm, A Density Functional Theory for the Average Electron Energy, *J. Chem. Theory and Comput.* **19**, 799 (2023).
- [115] S. Baroni, S. de Gironcoli, A. Dal Corso, and P. Giannozzi, Phonons and related crystal properties from density-functional perturbation theory, *Rev. Mod. Phys.* **73**, 515 (2001).
- [116] N. Marzari, A. A. Mostofi, J. R. Yates, I. Souza, and D. Vanderbilt, Maximally localized wannier functions: Theory and applications, *Rev. Mod. Phys.* **84**, 1419 (2012).
- [117] R. Sabatini, E. Küçükbenli, C. H. Pham, and S. de Gironcoli, Phonons in nonlocal van der Waals density functional theory, *Phys. Rev. B* **93**, 235120 (2016).
- [118] M. van Setten, M. Giantomassi, E. Bousquet, M. Verstraete, D. Hamann, X. Gonze, and G.-M. Rignanese, The pseudodojo: Training and grading a 85 element optimized norm-conserving pseudopotential table, *Comput. Phys. Commun.* **226**, 39 (2018).
- [119] G. Pizzi, V. Vitale, R. Arita, S. Blügel, F. Freimuth, G. Géranton, M. Gibertini, D. Gresch, C. Johnson, T. Koretsune, J. Ibañez-Azpiroz, H. Lee, J.-M. Lihm, D. Marchand, A. Marrazzo, Y. Mokrousov, J. I. Mustafa, Y. Nohara, Y. Nomura, L. Paulatto, S. Poncé, T. Ponweiser, J. Qiao, F. Thöle, S. S. Tsirkin,

- M. Wierzbowska, N. Marzari, D. Vanderbilt, I. Souza, A. A. Mostofi, and J. R. Yates, Wannier90 as a community code: new features and applications, *J. Phys.: Condens. Matter.* **32**, 165902 (2020).
- [120] O. Hassel, Die krystallstruktur des bornitrides, bn, *Nor. J. Geol.* **9**, 4 (1927), the original citation listed "9, 3, 4", interpreted here as Volume 9, Issue 3, Page 4. The journal is now known as *Norsk Geologisk Tidsskrift*.
- [121] L. Lui, Y. P. Feng, and Z. X. Shen, Structural and electronic properties of h-BN, *Phys. Rev. B* **68**, 104102 (2003).
- [122] R. S. Pease, An x-ray study of boron nitride, *Acta Crystallogr.* **5**, 356 (1952).
- [123] H. Rydberg, N. Jacobson, P. Hyldgaard, S. I. Simak, B. I. Lundqvist, and D. C. Langreth, Hard numbers on soft matter, *Surf. Sci.* **532–535**, 606 (2003).
- [124] J. Rohrer and P. Hyldgaard, Stacking and band structure of van der Waals bonded graphane multilayers, *Phys. Rev. B* **83**, 165423 (2011).
- [125] F. Gygi and A. Baldereschi, Self-consistent Hartree-Fock and screened-exchange calculations in solids: Application to silicon, *Phys. Rev. B* **34**, 4405 (1986).
- [126] R. M. Martin, *Electronic structure, Basic Theory and Practical Methods*, Vol. 28 (Cambridge University Press, 2004).
- [127] M. P. Tosi, Cohesion of Ionic Solids in the Born Model, in *Solid State Physics*, Vol. 16, edited by F. Seitz, D. Turnbull, and H. Ehrenreich (Academic Press, New York, 1964) p. 1.
- [128] X. Qian, F. Li, and H. Tian, Stacking effects on dynamic mechanical behavior of bilayer hexagonal boron nitride under impact, *Thin-Walled Struct.* **200**, 111866 (2024).
- [129] N. Ooi, V. Rajan, J. Gottlieb, Y. Catherine, and J. B. Adams, Structural properties of hexagonal boron nitride, *Model. Simul. Mater. Sci. Eng.* **14**, 515 (2006).
- [130] X. Blase, A. Rubio, S. G. Louie, and M. L. Cohen, Quasiparticle band structure of bulk hexagonal boron nitride and related systems, *Phys. Rev. B* **51**, 6868 (1995).
- [131] B. Arnaud, S. Lebègue, P. Rabiller, and M. Alouani, Huge Excitonic Effects in Layered Hexagonal Boron Nitride, *Phys. Rev. Lett.* **96**, 026402 (2006).
- [132] S. Grimme, J. Antony, S. Ehrlich, and H. Krieg, A consistent and accurate ab initio parametrization of density functional dispersion correction (DFT-D) for the 94 elements H–Pu, *J. Chem. Phys.* **132**, 154104 (2010).
- [133] T. Sohler, M. Calandra, and F. Mauri, Density functional perturbation theory for gated two-dimensional heterostructures: Theoretical developments and application to flexural phonons in graphene, *Phys. Rev. B* **96**, 075448 (2017).
- [134] J. Kleis, E. Schröder, and P. Hyldgaard, Nature and strength of bonding in a crystal of semiconducting nanotubes: van der Waals density functional calculations and analytical results, *Phys. Rev. B* **77**, 205422 (2008).
- [135] J. Tao, Y. Jiao, Y. Mo, Z.-H. Yang, J.-X. Zhu, P. Hyldgaard, and J. P. Perdew, First-principles study of the binding energy between nanostructures and its scaling with system size, *Phys. Rev. B* **97**, 155143 (2018).
- [136] C. Frostenson, P. A. T. Olsson, and P. Hyldgaard, Polyvinyl fluoride: Predicting polarization in a complex soft matter system, *Phys. Rev. Materials* **8**, 115603 (2024).
- [137] J. O. Sofo, A. S. Chaudhari, and G. D. Barber, Graphane: A two-dimensional hydrocarbon, *Phys. Rev. B* **75**, 165423 (2007).
- [138] D. C. Langreth, B. I. Lundqvist, S. D. Chakarova-Käck, V. R. Cooper, M. Dion, P. Hyldgaard, A. Kelkkanen, J. Kleis, L. Kong, S. Li, P. G. Moses, E. Murray, A. Puzder, H. Rydberg, E. Schröder, and T. Thonhauser, A density functional for sparse matter, *J. Phys.: Condens. Matter.* **21**, 084203 (2009).
- [139] A. L. Kutepov, Electronic structure of van der Waals ferromagnet CrI₃ from self-consistent vertex corrected GW approaches, *Phys. Rev. Mater.* **5**, 083805 (2021).
- [140] M. Wen, V. Abraham, G. Harsha, A. Shee, K. B. Whalley, and D. Zgid, Comparing Self-Consistent GW and Vertex-Corrected G₀W₀ (G₀W₀Γ) Accuracy for Molecular Ionization Potentials, *J. Chem. Theory Comput.* **20**, 3109 (2024).
- [141] K. Patkowski, Recent developments in symmetry-adapted perturbation theory, *WIREs. Comput. Mol. Sci.* **10**, e1452 (2020).
- [142] K. Szalewicz and B. Jeziorski, Symmetry-adapted double-perturbation analysis of intramolecular correlation effects in weak intermolecular interactions, *Mol. Phys.* **38**, 191 (1979).